A Multiscale Pressure Splitting of the Shallow-Water Equations

I. Formulation and 1D Tests

Olivier Le Maître,* Julia Levin,† Mohamed Iskandarani,‡ and Omar M. Knio§

CEMIF, Université d'Evry Val d'Essonne, 91020 Evry Cedex, France; †Institute of Marine and Coastal Sciences, Rutgers University, New Brunswick, New Jersey 08903-0231; ‡Rosenstiel School of Marine and Atmospheric Science, 4600 Rickenbacker Causeway, University of Miami, Miami, Florida 33149-1098; and §Department of Mechanical Engineering, The Johns Hopkins University, Baltimore, Maryland 21218-2686

Direct representation of the free surface in ocean circulation models leads to a number of computational difficulties that are due to the fast time scales associated with free-surface waves. These fast time scales generally result in severe time-step restrictions when the free surface is advanced using an explicit scheme and may result in large phase errors when the free surface is treated implicitly with a large time step. A multiple-scale analysis of the shallow-water equations is used to analyze this stiffness and to guide the construction of a computational methodology that overcomes the associated difficulties. Specifically, we explore a class of fractional step methods that utilize coarsened grids in the propagation of long-wave data. The behavior of the corresponding schemes is examined in detail in light of one-dimensional model problems, based on finite-difference or spectral-element discretizations. © 2001 Academic Press

Key Words: ocean circulation; aymptotic analysis; filtering; spectral elements; operator splitting.

1. INTRODUCTION

The ocean is subject to numerous forcing agents (e.g., tides, wind stress, solar radiation) with widely varying spatial (a few meters to thousand of kilometers) and temporal scales (minutes to decades). The ocean's response to these forcing mechanisms exhibits similarly broad spatial and temporal spectra. The fastest such response relevant to physical oceanographic processes are gravity waves that travel on the surface of the ocean at speeds exceeding 200 m/s in deep waters. Gravity waves carry energy and momentum across

large distances with little damping and thus allow a localized disturbance to propagate its influence over a large region.

The evolution of free-surface waves in ocean simulations leads to a number of computational difficulties. One of these difficulties concerns the nonlinear evolution of the free surface whose location is unknown a priori and must be computed as part of the solution. Another—more pronounced—example is the great disparity between the gravity wave speed and the characteristic advection velocity, which typically does not exceed 1–2 m/s. This disparity is usually expressed by the fact that the Froude number, defined as the ratio of advection velocity to gravity wave speed, is very small. As a consequence, free-surface models using explicit integration schemes (which are generally subject to a CFL time-step limit based on the highest wave speed) are restricted to time steps several orders of magnitude smaller than the time scale of phenomena of interest. As a result, extended high-resolution ocean simulations, such as those needed to model the mesoscale circulation, are expensive.

Ocean models have traditionally relied on the rigid-lid assumption [1, 2] to circumvent the computational difficulties of low-Froude-number free-surface flow. Fast gravity waves are thus suppressed and longer time steps can be used. This benefit comes at the cost of compensating for the rigid-lid assumption, either by computing a sea-surface pressure from the depth-integrated equations [3] or by solving a vorticity–streamfunction equation for the depth-averaged flow [1, 2].

Several difficulties hinder the usefulness of the streamfunction–vorticity formulation. One is the need to specify vorticity boundary conditions. Another difficulty arises for multiply connected domains, where additional integral conditions must be derived in order to determine streamfunction values around islands. The island conditions in particular complicate the solution process and inhibit parallelization of the model [3]. The sea-surface pressure formulation avoids the computational disadvantages of the streamfunction formulation. However, it too requires derived boundary conditions for the surface pressure. The biggest limitation of both approaches is that they treat the surface variable, the streamfunction in the streamfunction–vorticity formulation and sea-surface pressure in the latter formulation, as a diagnostic variable which inhibits the assimilation of satellite altimetry data in rigid-lid ocean models [4].

From a physical point of view, an evolution equation for the sea-surface displacement is highly desirable. First, it significantly simplifies the process of assimilating satellite altimetry data in ocean models. Such assimilation has proven to be extremely valuable in improving the models' performance since they integrate in the model a continuous, global, and spatially dense data set. Second, it allows the simulation of high-frequency dynamics, such as tides, that would otherwise be excluded under the rigid-lid assumption. These high-frequency dynamics can play an important role in transferring energy between the external and interior modes of the ocean, in the evolution of internal tides, in enhancing the dissipation of energy via enhanced bottom drag, and so forth.

To avoid otherwise prohibitive computation costs, it is imperative in free-surface models to separate the integration of the gravity waves, also referred to as fast modes, from the remaining dynamics. To this end, the three-dimensional governing equations are integrated vertically. The resulting depth-averaged equations, referred to as the shallow-water equations or the barotropic equations, contain the fast modes (e.g., [5, 6]). The shallow-water equations are coupled to the original set of equations through the nonlinear advection terms which link the slow and fast modes.

One approach to integrating the two- and three-dimensional equations is the so-called split-explicit method: the depth-mean equations are subtracted from the original three-dimensional equations to obtain the baroclinic equations which govern the three-dimensional evolution of the slow modes. The two-dimensional equations are advanced explicitly in time using a small time step dictated by the fast modes, while the three-dimensional equations are advanced with a larger time step (e.g., [7]). This asynchronous integration complicates the coupling of the fast and slow modes and must be filtered temporally in order to suppress a weak instability [8].

Synchronous large-time-step integration of the equations can be performed if a semi-implicit scheme is adopted for the two-dimensional equations (e.g., [9, 10]). The semi-implicit formulation generates a set of simultaneous equations which must be solved efficiently in order to keep the overall cost of the simulation at a reasonable level. The geometric complexity of ocean basins precludes the application of specialized direct solvers, such as fast Fourier methods. Thus, direct solvers are restricted to matrix-based techniques which are cost-effective when the size of the problem is small. However, when the size of the problem increases, the performance of direct matrix-based solvers deteriorates, primarily because of excessive memory requirements and to some extent poor scalability properties. Thus, for large problems, the application of iterative solvers is a more viable approach. Their effectiveness hinges on keeping the number and cost of iterations small.

Unfortunately, a large-time-step implicit treatment of the fast modes generally leads to undesirable side effects, including excessive damping and/or aliasing of the waves. Thus, irrespective of the solution approach and iteration cost, straightforward application of semi-implicit schemes may not necessarily yield a significant improvement over split-explicit schemes.

Our objective herein is to improve the treatment of fast surface gravity waves in ocean models. The new algorithms proposed target the models' ability to integrate the fast gravity modes accurately and efficiently during long-term simulations. We focus our attention exclusively on the solution of the shallow-water equations, which are the equations solved during the fast wave update. Our new approach is inspired by Klein's recent multiple-scale analysis of the weakly compressible Euler equations [11]. This analysis has led to a multiple-pressure-variable (MPV) low-Mach-number simulation scheme with features analogous to those desired.

The present article is organized as follows. In Section 2, we exploit the similarities between the shallow-water equations and the equations of gas dynamics, where the Mach number is the analogue of the Froude number, to adapt the results and methodology of [11] to the shallow-water equations. Based on the multiple-scale methodology, we outline in Section 3 the splitting of the shallow-water equations into three subsystems which are integrated via a fractional step approach. The splitting is based on (a) performing a fractional step update of advection and external forcing, (b) defining/extracting long-wave data using a filtering procedure, (c) propagating long-wave data using an explicit scheme on a coarsened grid, (d) interpolating the preliminary long-wave update onto the fine grid, and (e) finally performing an implicit short-wave update. We have implemented our scheme using two different spatial discretization schemes in order to demonstrate the generality of our approach. The first implementation relies on finite differences and is used in Section 4 to test various aspects of the algorithm, including the splitting, filtering, and interpolation procedures. Spectral-element discretization [12] is then introduced in Section 5, and the computations are extended to variable bathymetry and fixed wall conditions. We restrict

our attention to the splitting formulation and 1D tests; multidimensional implementation and numerical tests that include fast *and* slow modes will be discussed elsewhere [13]. Major conclusions are summarized in Section 6.

2. ASYMPTOTIC ANALYSIS OF THE SHALLOW-WATER EQUATIONS

2.1. Governing Equations

As mentioned in the Introduction, we focus on a reduced ocean circulation model that is based on the 2D shallow-water equations

$$\frac{\partial \tilde{U}}{\partial \tilde{t}} + \tilde{U} \cdot \tilde{\nabla}\tilde{U} + \tilde{g}\tilde{\nabla}\tilde{\zeta} = \tilde{b} \tag{1a}$$

$$\frac{\partial \tilde{\zeta}}{\partial \tilde{t}} + \tilde{\nabla} \cdot [(\tilde{h} + \tilde{\zeta})\tilde{U}] = 0, \tag{1b}$$

where $\tilde{U}$ is the depth averaged velocity, $\tilde{g}$ is the gravitational acceleration, $\tilde{\zeta}$ is the free-surface displacement, $\tilde{h}$ is the rest depth, and $\tilde{b}$ is a general forcing term, which include, among other things, wind stresses, Coriolis force, and dissipation. Tildes are used to denote dimensional quantities. Equation (1) must be supplemented with adequate boundary and initial conditions, which will be discussed later.

The above system of equations is obtained by depth-averaging the three-dimensional equations of motion, which should generally be used in modeling slow internal motions. The "reduced" system (1), however, is suitable for the present study, which focuses on the treatment of fast free-surface waves.

2.2. Relevant Scales and Normalization

In order to facilitate the analysis, the governing equations are first normalized. For ocean circulation problems of interest to the present work, the horizontal length scale $\tilde{L}_{ref}$ is on the order of 1000 km, the vertical length scale $\tilde{H}_{ref}$ is on the order of 1 km, and the characteristic advection velocity $\tilde{U}_{ref}$ is on the order of 1 m/s or smaller. Using the characteristic advection velocity and horizontal length scale, one can form a characteristic time scale, $\tilde{T}_{ref} \equiv \tilde{L}_{ref}/\tilde{U}_{ref}$. With the present choices of characteristic length, time, and velocity scales, the governing equations are normalized as

$$\frac{\partial u}{\partial t} + u \cdot \nabla u + \frac{1}{\epsilon^2}\nabla\zeta = b \tag{2a}$$

$$\frac{\partial \zeta}{\partial t} + \nabla \cdot [(h + \zeta)u] = 0, \tag{2b}$$

where $u \equiv \tilde{U}/\tilde{U}_{ref}$, $t \equiv \tilde{t}/\tilde{T}_{ref}$, $h \equiv \tilde{h}/\tilde{H}_{ref}$, $\zeta \equiv \tilde{\zeta}/\tilde{H}_{ref}$, $b \equiv \tilde{b}\tilde{L}_{ref}/\tilde{U}_{ref}^2$, and $\nabla \equiv \tilde{L}_{ref}\tilde{\nabla}$. Note that the normalization procedure leads to the definition of a dimensionless parameter, $\epsilon^2 \equiv \tilde{U}_{ref}^2/(\tilde{g}\tilde{H}_{ref})$. The ϵ is in fact the Froude number, and the inequality $\epsilon \ll 1$ expresses the fact that the characteristic advection velocity is much smaller than the speed of free-surface gravity waves; in deep water, for example, the Froude number is about 5×10^{-3}.

2.3. Expansions and Analysis

The above normalization suggests the following multiple-scale asymptotic expansion for surface elevation and velocity,

$$\zeta(\boldsymbol{x}, \xi, t) = \zeta^{(0)}(\boldsymbol{x}, \xi, t) + \epsilon \zeta^{(1)}(\boldsymbol{x}, \xi, t) + \epsilon^2 \zeta^{(2)}(\boldsymbol{x}, \xi, t) + \cdots \tag{3}$$

$$\boldsymbol{u}(\boldsymbol{x}, \xi, t) = \boldsymbol{u}^{(0)}(\boldsymbol{x}, \xi, t) + \epsilon \boldsymbol{u}^{(1)}(\boldsymbol{x}, \xi, t) + \epsilon^2 \boldsymbol{u}^{(2)}(\boldsymbol{x}, \xi, t) + \cdots, \tag{4}$$

where we have introduced the stretched spatial variable

$$\xi \equiv \epsilon \boldsymbol{x}. \tag{5}$$

We shall treat $\boldsymbol{x}$ and ξ as independent variables. As will be evident later, the variable ξ is most helpful in the description of long waves. Note that the resting depth h is independent of time and of ϵ; however, h may vary on the long-wave ξ-scale and may also exhibit small-scale $\boldsymbol{x}$ variations.

The normalization and multiple-scale expansions introduced above enable us to immediately adapt well-known results for zero- and low-Mach-number flow [11, 14–17]. In particular, following an approach similar to that in [11], it may be shown that:

1. The multiple-scale expansion introduced above leads to the following decomposition of the gradient operator,

$$\nabla = \nabla_x + \epsilon \nabla_\xi, \tag{6}$$

and to a hierarchy of perturbation equations. Of particular interest to the present discussion are the leading, first- and second-momentum equations, respectively,

$$\nabla_x \zeta^{(0)} = 0 \tag{7}$$

$$\nabla_x \zeta^{(1)} + \nabla_\xi \zeta^{(0)} = 0 \tag{8}$$

$$\frac{\partial \boldsymbol{u}^{(0)}}{\partial t} + \boldsymbol{u}^{(0)} \cdot \nabla_x \boldsymbol{u}^{(0)} + \nabla_x \zeta^{(2)} = \boldsymbol{b}^{(0)} - \nabla_\xi \zeta^{(1)}, \tag{9}$$

and the leading and first mass conservation equations, respectively,

$$\nabla_x \cdot \left[(h + \zeta^{(0)}) \boldsymbol{u}^{(0)} \right] = -\frac{\partial \zeta^{(0)}}{\partial t} \tag{10}$$

$$\frac{\partial \zeta^{(1)}}{\partial t} + \nabla_x \cdot \left[(h + \zeta^{(0)}) \boldsymbol{u}^{(1)} + \zeta^{(1)} \boldsymbol{u}^{(0)} \right] + \nabla_\xi \cdot \left[(h + \zeta^{(0)}) \boldsymbol{u}^{(0)} \right] = 0. \tag{11}$$

2. From Eq. (7), it follows immediately that the leading-order surface deformation is independent of $\boldsymbol{x}$. By considering the volume average of Eq. (8), assuming that $\zeta^{(1)}$ has at most sublinear growth [11], and combining with the result just stated, we conclude that $\zeta^{(0)}$ is independent of ξ as well and is consequently a function of time only. It also follows that the first-order surface displacement does *not* admit small-scale variations, i.e., $\zeta^{(1)} = \zeta^{(1)}(\xi, t)$.

3. As shown in Eq. (10), temporal variations of the leading-order surface elevation impose a divergence constraint on the flow field. The significance of this constraint becomes more

obvious after we integrate this relationship over the area of the basin and apply the divergence theorem to obtain

$$\frac{\partial \zeta^{(0)}}{\partial t} = -\frac{1}{\mathcal{A}} \int_{\mathcal{L}} (h + \zeta^{(0)}) \boldsymbol{u}^{(0)} \cdot \boldsymbol{n} \, d\sigma, \tag{12}$$

where $\mathcal{A}$ is the area of the basin, $\mathcal{L}$ its perimeter, $\boldsymbol{n}$ the local outer normal, and $d\sigma$ a length element. Thus, $\zeta^{(0)}$ changes due to net mass into the basin.

4. When the area of the basin $\mathcal{A}$ is large, as is obviously the case in most ocean applications, the system supports nontrivial wave motion, and we may assume that $\zeta^{(0)}$ vanishes identically. In this case, net mass into the basin is instead reflected through mean changes of $\zeta^{(1)}$. Thus, global changes in the depth, if relevant, are "felt" by the cumulative effect of gravity waves; see related discussion in [11] and additional remarks in item (5) below.

5. To analyze the dynamics of the system further, we introduce a spatial averaging operator which filters out small-scale fluctuations. We shall use the overbar to denote this filtering operator whose action shall be specified later. Taking the average of Eq. (11), and noting that $\overline{\zeta^{(1)}} = \zeta^{(1)}$, we get

$$\frac{\partial \zeta^{(1)}}{\partial t} + \nabla_\xi \cdot \overline{\left[(h + \zeta^{(0)}) \boldsymbol{u}^{(0)} \right]} = 0. \tag{13}$$

The spatial average of the divergence term can be estimated from (9), which we rewrite in the conservation form

$$\frac{\partial (h + \zeta^{(0)}) \boldsymbol{u}^{(0)}}{\partial t} + \nabla_x \cdot \left[(h + \zeta^{(0)}) \boldsymbol{u}^{(0)} \boldsymbol{u}^{(0)} \right] + (h + \zeta^{(0)}) \nabla_x \zeta^{(2)}$$
$$= (h + \zeta^{(0)}) \boldsymbol{b}^{(0)} - (h + \zeta^{(0)}) \nabla_\xi \zeta^{(1)} \tag{14}$$

after using Eq. (10); the term $\boldsymbol{u}^{(0)} \boldsymbol{u}^{(0)}$ denotes a dyadic product. The second term on the left-hand side of the above equation drops out upon spatial averaging:

$$\frac{\partial \overline{(h + \zeta^{(0)}) \boldsymbol{u}^{(0)}}}{\partial t} + \overline{(h + \zeta^{(0)}) \nabla_x \zeta^{(2)}} = \overline{(h + \zeta^{(0)}) \boldsymbol{b}^{(0)}} - \overline{(h + \zeta^{(0)}) \nabla_\xi \zeta^{(1)}}. \tag{15}$$

Equations (15) and (13) can be combined to yield

$$\frac{\partial^2 \zeta^{(1)}}{\partial t^2} - \nabla_\xi \cdot \left[\bar{h} \nabla_\xi \zeta^{(1)} \right] = \nabla_\xi \cdot \left(\overline{h \nabla_x \zeta^{(2)}} \right) - \nabla_\xi \cdot \overline{h \boldsymbol{b}^{(0)}}, \tag{16}$$

after setting $\zeta^{(0)} = 0$ (per point 4). Thus, the large-scale $O(\epsilon)$ component of the surface displacement obeys the linear inhomogeneous wave equation, with variable wave speed $c(\xi) = \sqrt{\bar{h}(\xi)}$. Note that the correlation $\overline{h \nabla_x \zeta^{(2)}}$ vanishes whenever h varies on the ξ-scale only.

6. The discussion above indicates that long-wave "data" are responsible for fast waves with propagation speeds that are $O(1)$ on the ξ-scale. To further appreciate this result, we revert to standard notation by replacing ∇_ξ with $\epsilon^{-1} \nabla$ (see Eq. (6)), and thus convert Eq. (16) into

$$\frac{\partial^2 \zeta^{(1)}}{\partial t^2} - \nabla \cdot \left[\frac{\bar{h}}{\epsilon^2} \nabla \zeta^{(1)} \right] = \frac{1}{\epsilon} \nabla \cdot \left(\overline{h \nabla \zeta^{(2)}} \right) - \frac{1}{\epsilon} \nabla \cdot \overline{h \boldsymbol{b}^{(0)}}. \tag{17}$$

Thus, in the usual coordinate frame (x), wave propagation speeds are $O(\epsilon^{-1})$. Note that by virtue of our normalization conventions the particle motion has characteristic speeds that are $O(1)$ on the x scale. As noted earlier, the disparity between the characteristic speed of advective motion and the characteristic wave propagation speeds underscores one of the well-known difficulties in modeling low-Froude-number flows.

3. SPLITTING OF THE SHALLOW-WATER EQUATIONS

3.1. Preliminaries

The multiple-scale analysis conducted above suggests that a good starting point for addressing the difficulties of the low-Froude-number problem is to (a) isolate fast-moving gravity waves from the remaining phenomena, and (b) absorb the difficulties associated with the fast waves by first performing a long-wave integration based on suitably averaged data and then accounting for small-scale dynamics. An attractive approach which reflects these ideas is to perform a splitting of the equations of motion into slow and fast dynamics.

We begin our presentation by rewriting the equations in time-integrated form,

$$\boldsymbol{u}(t_{n+1}) = \boldsymbol{u}(t_n) + \int_{t_n}^{t_{n+1}} [\boldsymbol{b} - \boldsymbol{u} \cdot \nabla \boldsymbol{u} - \epsilon^{-2} \nabla \zeta] \, dt \qquad (18)$$

$$\zeta(t_{n+1}) = \zeta(t_n) - \int_{t_n}^{t_{n+1}} \nabla \cdot [(h + \zeta)\boldsymbol{u}] \, dt, \qquad (19)$$

where we assume that the initial conditions at time t_n are known. The above time integral can be split into two systems, one corresponding to the slow dynamics,

$$\boldsymbol{u}_i = \boldsymbol{u}(t_n) + \int_{t_n}^{t_{n+1}} [\boldsymbol{b} - \boldsymbol{u} \cdot \nabla \boldsymbol{u}] \, dt \qquad (20)$$

$$\zeta_i = \zeta(t_n) - \int_{t_n}^{t_{n+1}} \nabla \cdot (\zeta \boldsymbol{u}) \, dt, \qquad (21)$$

and another corresponding to the fast dynamics,

$$\boldsymbol{u}(t_{n+1}) = \boldsymbol{u}_i - \int_{t_n}^{t_{n+1}} \epsilon^{-2} \nabla \zeta \, dt \qquad (22)$$

$$\zeta(t_{n+1}) = \zeta_i - \int_{t_n}^{t_{n+1}} \nabla \cdot (h\boldsymbol{u}) \, dt, \qquad (23)$$

where $\boldsymbol{u}_i$ and ζ_i denote intermediate values. Note that the fast system corresponds to solving the linear differential equations

$$\frac{\partial \boldsymbol{u}}{\partial t} + \epsilon^{-2} \nabla \zeta = 0 \qquad (24)$$

$$\frac{\partial \zeta}{\partial t} + \nabla \cdot (h\boldsymbol{u}) = 0 \qquad (25)$$

with the initial conditions pair $(\boldsymbol{u}_i, \zeta_i)$.

Guided by the asymptotic analysis, we extract the long-wave data using the large-scale averaging operator [11, 14]

$$\bar{f}(x) \equiv \int_{\mathcal{D}(x;L)} f(x) W(x) \, d\mathcal{A}, \tag{26}$$

where W denotes a "radial" weight function of compact support, and $\mathcal{D}$ is the support of W. The notation $\mathcal{D}(x; L)$ is used to indicate that the support of W is centered at x and has characteristic size L. The choice of W and L will be discussed further below.

The averaging operator isolates the long- and short-gravity-wave dynamics into separate systems:

$$\frac{\partial \bar{u}}{\partial t} + \epsilon^{-2} \nabla \bar{\zeta} = 0 \tag{27}$$

$$\frac{\partial \bar{\zeta}}{\partial t} + \nabla \cdot \overline{hu} = 0. \tag{28}$$

Note that the above ("linearized") system accounts for fast-wave propagation. By integrating it in an implicit fashion, or by using an explicit solver on a *coarse* computational grid, it is possible to avoid the stiff CFL conditions which limit the application of conventional solvers. As will be discussed later, the coarse-grid approach is preferred as it also avoids aliasing or excessive damping of the long waves. The asymptotic analysis leads us to associate the averaged pressure $\bar{\zeta}$ with $\epsilon \zeta^{(1)}$; the short-wave perturbations can then be defined as $\epsilon^2 \zeta^{(2)} = \zeta - \epsilon \zeta^{(1)}$.

The equations governing the short-wave propagation can be obtained simply by subtracting system (27)–(28) from system (24)–(25),

$$\frac{\partial (u - \bar{u})}{\partial t} + \epsilon^{-2} \nabla (\zeta - \bar{\zeta}) = 0 \tag{29}$$

$$\frac{\partial (\zeta - \bar{\zeta})}{\partial t} + \nabla \cdot [(hu - \overline{hu})] = 0, \tag{30}$$

or equivalently,

$$\frac{\partial u}{\partial t} + \nabla \zeta^{(2)} = \frac{\partial \bar{u}}{\partial t} \tag{31}$$

$$\epsilon^2 \frac{\partial \zeta^{(2)}}{\partial t} + \nabla \cdot (hu) = -\epsilon \frac{\partial \zeta^{(1)}}{\partial t}. \tag{32}$$

For the numerical scheme to survive the zero Froude number limit, $\epsilon \to 0$, the pressure term in the momentum equation should be treated implicitly, or at least in a semi-implicit fashion. Choosing the former approach, we rewrite the above system in the semi-discrete form,

$$\mathcal{M} u^{n+1} + \nabla \zeta^{(2)} = P \tag{33}$$

$$\epsilon^2 \frac{\delta \zeta^{(2)}}{\delta t} + \nabla \cdot (hu^{n+1}) = \epsilon Q, \tag{34}$$

where $\mathcal{M}$ is a time-discretization matrix, and P and Q denote the right-hand-side terms in Eqs. (31) and (32) after time discretization, respectively. Combining Eqs. (33) and (34)

results in the following "pressure" equation:

$$\epsilon^2 \frac{\delta \zeta^{(2)}}{\delta t} - \nabla \cdot [h \mathcal{M}^{-1} \nabla \zeta^{(2)}] = -\nabla \cdot [h \mathcal{M}^{-1} P] + \epsilon Q. \tag{35}$$

Note that in the limit $\epsilon \to 0$, the above equation reduces to an elliptic equation for the second-order pressure $\zeta^{(2)}$, which coincides with the familiar "projection" step encountered in the rigid-lid formulation.

Also note that, without the multiple pressure approach which explicitly separates $O(\epsilon)$ (long gravity wave) and $O(\epsilon^2)$ (advection) contributions, the analogue of Eq. (35) would read

$$\epsilon^2 \frac{\delta \zeta}{\delta t} - \nabla \cdot [h \mathcal{M}^{-1} \nabla \zeta] = -\epsilon^2 \nabla \cdot [h \mathcal{M}^{-1} P]. \tag{36}$$

In the limit $\epsilon \to 0$, Eq. (36) reduces to a homogeneous elliptic equation in ζ, with no dependence on the velocity field. Obviously, this is **not** the correct low-Froude-number limit. It follows from the above discussion that the definition of multiple pressure fields, appropriately scaled by different powers of ϵ, is a key ingredient for the present shallow water scheme to survive in the low-Froude-number limit.

3.2. Numerical Implementation

Following the discussion above, we explore a splitting method for integration of the shallow-water equations. The splitting is based on using a filtering operator to decompose the numerical solution into small- and large-scale components, which are advanced separately on a fine and a coarse grid, respectively. Accordingly, the numerical scheme incorporates the fractional steps summarized below. To emphasize the general nature of the approach, we revert to the original **dimensional form** of the equations, but to simplify the notation we will drop the tildes from dimensional symbols.

S1. *Advection and External Forcing*

In the first step, we account for advection processes and external forcing on the system by integrating the system

$$\textbf{System I:} \quad \begin{cases} \frac{\partial U}{\partial t} = -U \cdot \nabla U + b \\ \frac{\partial \zeta}{\partial t} = -\nabla \cdot (\zeta U) \end{cases} \tag{37}$$

with the initial conditions pair (U_n, ζ_n); here subscript n refers to the time level at the beginning of the integration step. An explicit scheme during this step does not cause computational difficulties, since the characteristic advection velocity is $O(1)$. Let U_i and ζ_i denote the resulting velocity and elevation at the end of S1.

S2. *Decomposition of the Intermediate Solution*

Guided by the asymptotic analysis, we rely on spatial filtering to decompose ζ_i and U_i into large-scale and small-scale components. We use

$$\zeta_i^l = \bar{\zeta}_i, \quad \zeta_i^s = \zeta_i - \bar{\zeta}_i \tag{38}$$

$$U_i^l = \bar{U}_i, \quad U_i^s = U_i - \bar{U}_i, \tag{39}$$

where the superscripts l and s refer to the large- and small-scale components, respectively, while the overbar refers to the averaging operator introduced in the previous section.

S3. *Long-Wave Integration*

The long-wave components ζ_i^l and U_i^l are used as initial values for the second intermediate step, which performs a long-wave update. The latter is obtained by integrating

$$\textbf{System II:} \quad \begin{cases} \frac{\partial U^l}{\partial t} + g\nabla \zeta^l = 0 \\ \frac{\partial \zeta^l}{\partial t} = -\nabla \cdot [hU^l]. \end{cases} \tag{40}$$

Note that since (40) accounts for fast-wave propagation, it has to be integrated in an implicit fashion or by using an explicit solver on a coarse computational grid. While both approaches enable us to overcome the stiff CFL restriction associated with fast waves, the latter approach is preferred because it naturally avoids aliasing and/or excessive damping. Nonetheless, both methods will be tested and compared. We let U_p^l and ζ_p^l denote the fields resulting from the above fractional step. When a coarse grid is used in the integration of (40), the large-scale field must be "interpolated" onto the fine grid for the solution to proceed. In this case, U_p^l and ζ_p^l refer to the fields after the interpolation is performed. Details on interpolation procedures will be discussed later.

We have implicitly assumed that the depth h varies on the large scale only, so that $(hU)^l = hU^l$. If h has small-scale variations, an additional term must be inserted to account for the generation of long waves from the interaction of small-scale waves with the small-scale topography, i.e., the term $\overline{h\nabla_x \zeta}^{(2)}$ in Eq. (16).

S4. *Small-Scale Integration*

The integration cycle is completed by integrating the small-scale pressure variations

$$\textbf{System III:} \quad \begin{cases} \frac{\partial U^s}{\partial t} + g\nabla \zeta^s = 0 \\ \frac{\partial \zeta^s}{\partial t} + \nabla \cdot (hU^s) = 0 \end{cases} \tag{41}$$

with U_i^s and ζ_i^s as initial data, and setting $U_{n+1} = U_p^l + U_p^s$ and $\zeta_{n+1} = \zeta_p^l + \zeta_p^s$. Note that in the limit $\epsilon \to 0$, System II is no longer needed while System III reduces to the familiar rigid-lid formulation. Since in this limit the speed of pressure waves diverges as ϵ^{-1}, the above system is integrated in an implicit fashion. Also note that while System III has a form very close to that of System II, the latter treats long-wave data with pressure amplitudes scaling as $O(\epsilon)$, while the former describes small-scale dynamics with pressure amplitudes scaling as $O(\epsilon^2)$.

Summary

We summarize the splitting algorithm steps as follows:

1. Integrate (37) explicitly using (U_n, ζ_n) as initial conditions. Label the resulting fields (U_i, ζ_i).

2. Extract the long and short waves: $(U_i^l, \zeta_i^l) = (\bar{U}_i, \bar{\zeta}_i)$, and $(U_i^s, \zeta_i^s) = (U_i - U_i^l, \zeta_i - \zeta_i^l)$.

3. Integrate system (40) using $(\boldsymbol{U}_i^l, \zeta_i^l)$ as initial data and call the resulting fields $(\boldsymbol{U}_p^l, \zeta_p^l)$.
4. Integrate system (41) using $(\boldsymbol{U}_i^s, \zeta_i^s)$ as initial data and call the resulting fields $(\boldsymbol{U}_p^s, \zeta_p^s)$.
5. Set $(\boldsymbol{U}_{n+1}, \zeta_{n+1}) = (\boldsymbol{U}_p^l + \boldsymbol{U}_p^s, \zeta_p^l + \zeta_p^s)$, and go to step 1.

3.3. Remarks

1. It should be emphasized that in the approach described above, one is actually solving the **full** equations of motion and **not** a system of asymptotic conservation laws. The various splitting, filtering, and interpolation procedures are simply designed to help achieve a numerical shallow-water model which (a) would allow synchronous integration of the 2D and 3D equations, (b) would allow large time steps by overcoming the surface CFL condition, (c) does not damp or alias long waves, (d) accommodates large variation in the rest depth, and (e) would extend naturally from zero to moderate Froude numbers. In particular, the propagation of long-wave data on a coarsened grid (step S3) may be viewed as a "preconditioning" step and should not be identified with an approximate evolution equation.

2. As mentioned in the Introduction, an approach analogous to that described above has been used in the context of low-Mach-number finite-difference computations [11, 14, 18]. Based on these experiences, one would anticipate that the success of the present multiple-scale ocean modeling approach would crucially depend on the performance and cost of the averaging and interpolation operators, which are used to isolate different components of the solution and in transferring data between grids of different resolution. Below, we focus on these issues for finite-difference and spectral-element discretizations.

3. Another key aspect in the present approach is the implicit or semi-implicit pressure solution in the correction step, S4. Obviously, this small-scale pressure update must not require excessive overhead, so that the advantages of the time splitting can be maintained. The selection and implementation of adequate solvers will be addressed in a following article [13], in the context of multidimensional computations.

4. FINITE-DIFFERENCE COMPUTATIONS

In this section, we examine the performance of the splitting scheme of the previous section in a simplified one-dimensional setting. As discussed in Section 4.1, a test problem which consists purely of advection and gravity waves is considered. The problem is set in a 1D periodic domain of constant depth. This simplified setting is also used to analyze the role of the filtering operator that is used to extract the long-wave data. In particular, results obtained with various filter functions are contrasted to each other and to results of spectral-Fourier filtering and interpolation. Furthermore, we exploit the present setting to explore two approaches to long-wave integration. In the first approach, long waves are advanced using an implicit scheme on the fine grid; in the second, long waves are treated explicitly on a coarse grid. These approaches are referred to as single-grid method (SGM) and double-grid method (DGM) and are discussed in Sections 4.2 and 4.3, respectively.

4.1. Model Problem

In order to isolate gravity waves and advection, we focus on a shallow-water system with no external forcing. This is simply achieved by setting $\boldsymbol{b} \equiv 0$ in the governing equations. Using the reduced system, we consider a one-dimensional basin of length $L = L_{\text{ref}} = 3600\,\text{km}$,

and uniform rest depth, $h = H_{\text{ref}} = 1$ km. Periodic boundary conditions on the velocity and elevation are imposed, using

$$U(x = 0, t) = U(x = L_{\text{ref}}, t), \quad \zeta(x = 0, t) = \zeta(x = L_{\text{ref}}, t), \quad \forall t. \tag{42}$$

Unless otherwise noted, the initial conditions are given by

$$U(x, t = 0) = 0 \tag{43}$$

and

$$\zeta(x, t = 0) = \zeta_0(x) = a \exp\left[-\frac{\left(\frac{x}{L_{\text{ref}}} - \frac{1}{2} \right)^2}{0.005} \right]; \tag{44}$$

i.e., the velocity initially vanishes while the surface elevation corresponds to a Gaussian bump centered at the middle of the basin, and with amplitude $a = 0.5$ m.

The linear solution to the above problem consists of left- and right-going waves traveling at the speed $c = \sqrt{gh} \sim 100$ m/s. The linear solution is given by

$$\zeta(x, t) = \frac{1}{2}[\zeta_0(x - ct) + \zeta_0(x + ct)] \tag{45}$$

$$u(x, t) = \frac{g}{2c}[\zeta_0(x - ct) - \zeta_0(x + ct)]. \tag{46}$$

Thus, the Froude number can be estimated as $ga/c^2 = a/h \sim 5 \times 10^{-4}$.

4.2. Single-Grid Method

4.2.1. *Discretization*

In the SGM, the spatial discretization of the governing equations is performed on a single, staggered, finite-difference grid with mesh size Δx. The grid points are uniformly distributed over the interval $[0, L_{\text{ref}}]$. The grid size $\Delta x = L_{\text{ref}}/N_f$, where N_f is the total number of grid points. The velocity field is discretized at the node points while the elevation is discretized at cell centers. We adopt the standard notation $x_i \equiv (i - 1)\Delta x$, $x_{i+1/2} \equiv (x_i + x_{i+1})/2$, $U_i \equiv U(x_i)$, $\zeta_i \equiv \zeta(x_{i+1/2})$, and $i = 1, \ldots, N_f$. Derivative operators are approximated using centered differences, according to

$$\begin{aligned}
\frac{\partial U}{\partial x}(x_i) &= \frac{U_{i+1} - U_{i-1}}{2\Delta x} \\
\frac{\partial \zeta}{\partial x}(x_i) &= \frac{\zeta_i - \zeta_{i-1}}{\Delta x} \\
\frac{\partial (U\zeta)}{\partial x}(x_{i+1/2}) &= \frac{\frac{\zeta_{i+1} - \zeta_i}{2} U_{i+1} - \frac{\zeta_i + \zeta_{i-1}}{2} U_i}{\Delta x}.
\end{aligned} \tag{47}$$

As outlined in the previous sections, different integration schemes are used in the fractional step approach. In the present SGM implementation, we rely on the third-order Adams–Bashforth (AB3) scheme to integrate System I and on the Crank–Nicolson (CN) scheme to update Systems II and III.
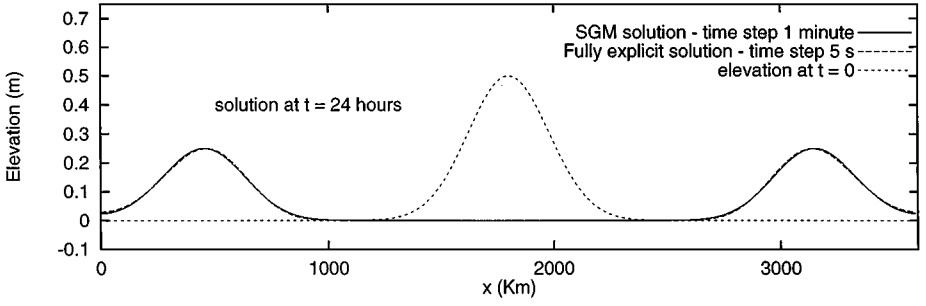
FIG. 1. Comparison of computed solutions after 1 day using the SGM and fully explicit schemes. The SGM computations are performed with $\Delta t = 1$ min, while the explicit scheme uses $\Delta t = 5$ s, $\Delta x = 10$ km in both cases.

4.2.2. *Results*

The evolution of the system is computed for a period of 1 day, using a grid with $N_f = 360$ grid points and a mesh size $\Delta x = 10$ km. In all cases discussed in the present section, the averaging procedure relies on a top-hat filter,

$$W_b(x) = \begin{cases} \frac{1}{2L_a} & |x| \leq L_a \\ 0 & |x| > L_a \end{cases}, \tag{48}$$

where L_a is the averaging length. For the tests below, we use $L_a = 1000$ km.

Figure 1 shows the elevation after 1 day, computed using a time step $\Delta t = 1$ min. The corresponding advective CFL number is $\text{CFL}_a = 10^{-3}$, while the CFL based on the gravity wave speed is $\text{CFL}_w = 0.6$. The SGM solution is contrasted with results based on a fully explicit integration of the *original* system of equations, using an AB3 scheme with $\Delta t = 5$ s. The agreement between the two solutions is quite evident.

Next, we examine the effect of the time step on the SGM predictions. To this end, solutions are obtained with $\Delta t = 2$, 5, and 10 min, and curves for the free-surface elevation at the end of 1 day are plotted in Fig. 2. The results show that for $\Delta t \geq 5$ min the SGM predictions are significantly influenced by the value of the time step. Rapid amplification of phase errors is observed as the time step increases.
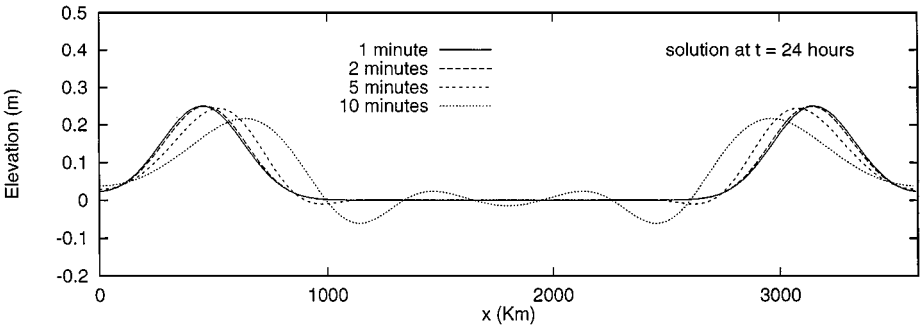

FIG. 2. Effect of Δt on SGM predictions. Plotted are free-surface elevations computed with $\Delta x = 10$ km, and $\Delta t = 1, 2, 5,$ and 10 min.
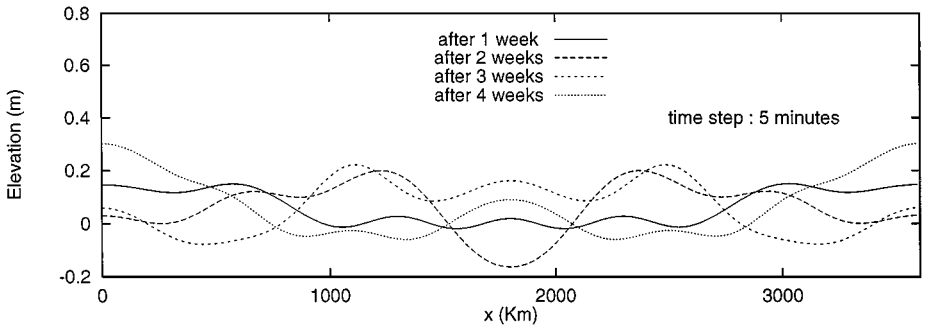
FIG. 3.   Free-surface elevation at selected times. The SGM solution is obtained with $\Delta x = 10$ km and $\Delta t = 5$ min.

To further verify this claim, we plot in Fig. 3 the free-surface elevation at 1-week intervals, the solution being computed with $\Delta t = 5$ min. The plot shows oscillations moving at different speeds, an indication of dispersive phase errors. Additional evidence regarding these phase errors can be found in Fig. 4, which shows the evolution of initially monochromatic free-surface waves. Figure 4 clearly shows that spurious frequencies are not generated. In addition, individual modes maintain their amplitudes, indicating that wave damping does not occur.

The present tests show that the split scheme introduced in the previous section is in fact well suited to shallow-water computations at low Froude number. However, the implicit treatment of long waves, though (neutrally) stable, may lead to large phase errors. These errors become excessively large as soon as the wave-CFL number, CFL_w, exceeds unity.
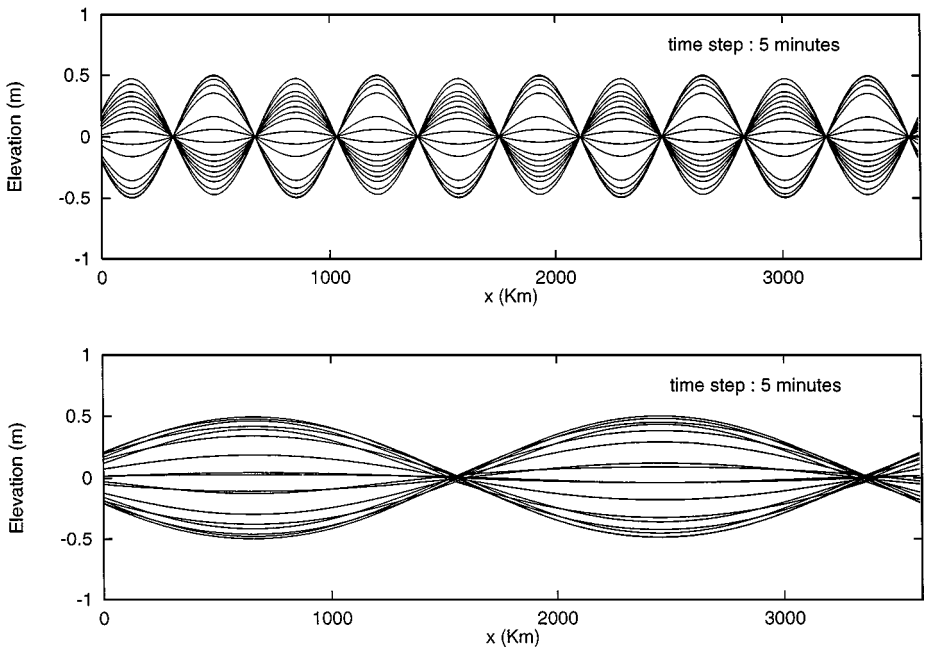

FIG. 4.   Free-surface elevation plotted at one-quarter-week intervals, for two different monochromatic waves. The SGM solution are obtained with $\Delta x = 10$ km and $\Delta t = 5$ min.

Consequently, the present approach does not appear to constitute a suitable means for constructing a large time-step scheme. This motivates us to consider the fine-/coarse-grid approach below as a possible alternative.

4.3. Double-Grid Method

As mentioned earlier, the DGM aims at defeating the wave-CFL restriction by using, in S3, a coarse grid in order to propagate the long-wave data. The remaining pieces of the algorithm in S1 and S4 are performed using the same spatial discretization as in the SGM and on a similar grid, which is now referred to as the fine grid. Thus, we shall only describe the data transfer procedure in S2 and the long-wave propagation in S3.

4.3.1. *Definition of Coarse Grid*

In the finite-difference computations, the coarse grid is defined so that averaging and interpolation procedures can be easily implemented. This is achieved using a construction which ensures that all the nodes of the coarse grid coincide with fine-grid nodes at the corresponding spatial locations. To this end, the coarse-grid size, ΔX, is defined using

$$\Delta X = n_r \Delta x, \tag{49}$$

where Δx is the fine mesh size. The term n_r is assumed to be an odd positive integer and is referred to as grid ratio. Thus, the number of grid points in the coarse grid, N_c, is given by $N_c = N_f / n_r$. The coarse-grid locations are related to the fine-grid positions using

$$\begin{cases} X_i = x_j, & j = (i-1)n_r + 1 \\ X_{i+1/2} = x_k, & k = (i-1/2)n_r + 1, \end{cases} \tag{50}$$

$i = 1, \ldots, N_c$. As discussed below, this definition simplifies the data transfer operations outlined below.

The choice of grid ratio is primarily dictated by the length scales of the slow and fast waves. If the latter are much longer than the former, the grid ratio should scale as the inverse of the Froude number; otherwise, the length scale of the fast waves imposes an upper limit. Thus we can write $\Delta X = \min(l/M, \Delta x/\epsilon)$, where l is the characteristic length of the fast waves, and M is the minimum number of grid cells needed to resolve it. In the example problem, it is the length scale of the fast wave that dictate the coarse-grid spacing, i.e., the width of the Gaussian bump which is 200 km.

4.3.2. *Filtering and Interpolation*

Data transfer between the fine and coarse grids is based on (a) interpolating the coarse grid data onto the fine grid, and (b) filtering fine-grid data to define smooth fields that are well represented on the coarse grid. Obviously, these steps should be carefully performed to avoid generating potentially harmful computational modes.

For the purpose of interpolating coarse-grid data the finite-difference computations rely exclusively on a Fourier interpolation procedure. The latter is based on representing the coarse data using Fourier modes and directly evaluating the Fourier representation on the fine-grid values. This ensures that (a) the interpolated field agrees with the original field at the coarse-grid locations, and (b) high-wavenumber modes are not spuriously generated.

While Fourier interpolation may not be immediately extended to more general situations, it enables us to focus on other aspects of the numerical construction. Alternatives are discussed in the following section, in the context of a spectral-element discretization.

Two procedures for extracting coarse-grid data from the corresponding fine fields are considered. The first is based on applying a filter function, as indicated in Eq. (26). In addition to the box filter defined in Eq. (48), we consider the second-order Gaussian filter

$$W_g(x) = \frac{1}{\sqrt{\pi}\sigma} \exp\left(-\frac{x^2}{\sigma^2}\right) \tag{51}$$

and an additional filter, W_d, that is designed to provide a more direct control on the spectrum of the large-scale component. W_d is defined as the inverse Fourier transform of the transfer function,

$$H(k) \equiv \begin{cases} 1 & k \le k_c \\ \exp\left[-\left(\frac{|k-k_c|}{n_c}\right)^n\right] & k > k_c, \end{cases} \tag{52}$$

where k_c is the cutoff wavenumber, n is the order of the Gaussian tail, and n_c is its width. H and W_d are plotted in Fig. 5 for $n = 2$ and different values of k_c and n_c.

In order to analyze the effects of filter size and shape, a second filtering approach that is based on a sharp spectral cutoff is used. This is simply implemented by taking the Fourier transform of the fine-grid data, truncating the spectrum at a cutoff wavenumber k_c, and then inverting the truncated spectrum onto the coarse-grid positions.

4.3.3. Long-Wave Propagation

We start the analysis of the DGM by comparing solutions obtained with an explicit and an implicit scheme in step S3. The third-order Runge–Kutta scheme (RK3) and the Crank–Nicolson scheme are used. The scheme is applied to the model problem summarized in Section 4.1. Computations are first performed using the filter function W_d with a cutoff wavenumber $k_c = 15$. The grids are set up so that the fine-mesh size $\Delta x = 10$ km and the coarse-grid size $\Delta X = 30$ km, i.e., the grid ratio $n_r = 3$. As shown in Fig. 6a for the present choice of k_c, the filtered and original signals coincide and the short-scale component vanishes. Also, for the present discretization, the large-scale component is well represented on the coarse grid, with approximately 8 grid points within the cutoff wavelength.

The evolution of the free surface during day 10 is plotted in Fig. 7, which shows solutions obtained with RK3 and CN, both using $\Delta t = 2$ min. The two solutions are directly compared in Fig. 8, which depicts the free-surface elevation at the end of day 10. The results show that the initial "bump" in the free-surface elevation gives rise to a right-moving wave and a left-moving wave, with short-wavelength ripples preceding and trailing their crests. These ripples are caused by phase error that leads to dispersion. Since the gravity wave speed is approximatively 100m/s, at the end of day 10, the right- and left-moving waves have completed 26 round trips along the basin. Moreover, further analysis shows that the RK3 scheme introduces less dispersion than the CN scheme. This difference can be seen in Fig. 8, where the solution obtained using the RK3 scheme has preserved the wave shape better than the CN scheme. The results also show that wave attenuation is very weak throughout the computation; energy transfer to short waves is also insignificant. Note that for the same time step and fine-mesh size, the SGM solution rapidly breaks down because of buildup
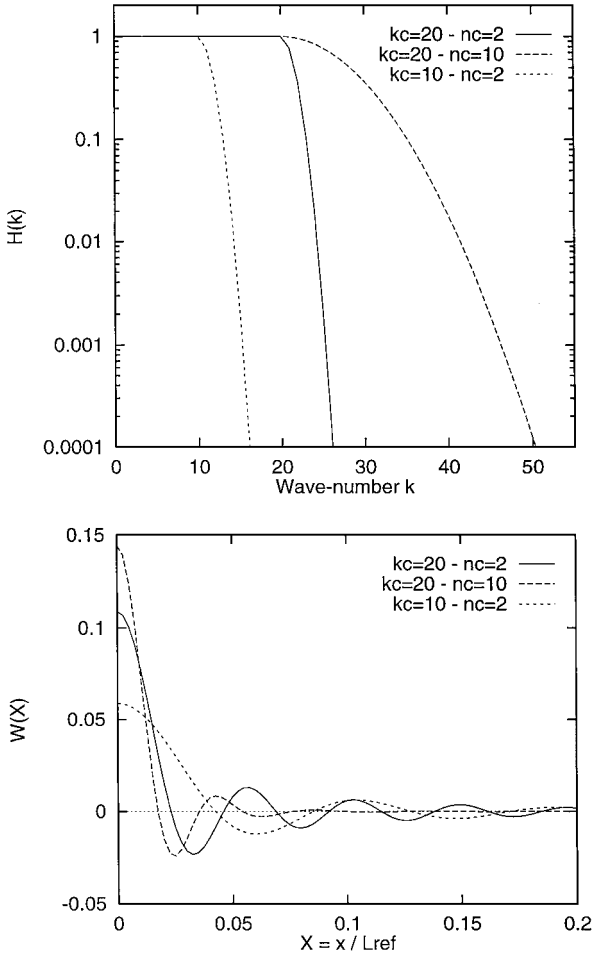
FIG. 5. Curves for H (top) and W_d (bottom) for $n = 2$, and different values of k_c and n_c.

of phase errors. Thus, the double-grid scheme provides an approach more suitable for the construction of the large-time-step method.

The Crank–Nicolson and RK3 solutions are further compared in Figs. 9 and 10, which show simulations using the same model problem and spatial resolutions but with a larger time
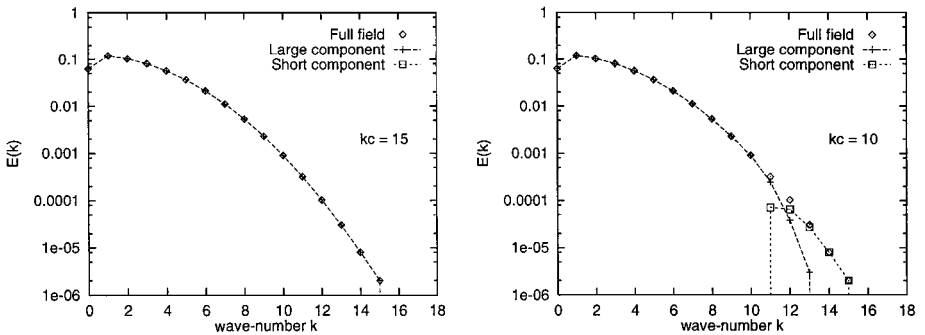

FIG. 6. Application of the filter W_d to the initial elevation field in Eq. (42). Full, filtered, and short-scale spectra with $k_c = 15$ (left) and $k_c = 10$ (right).
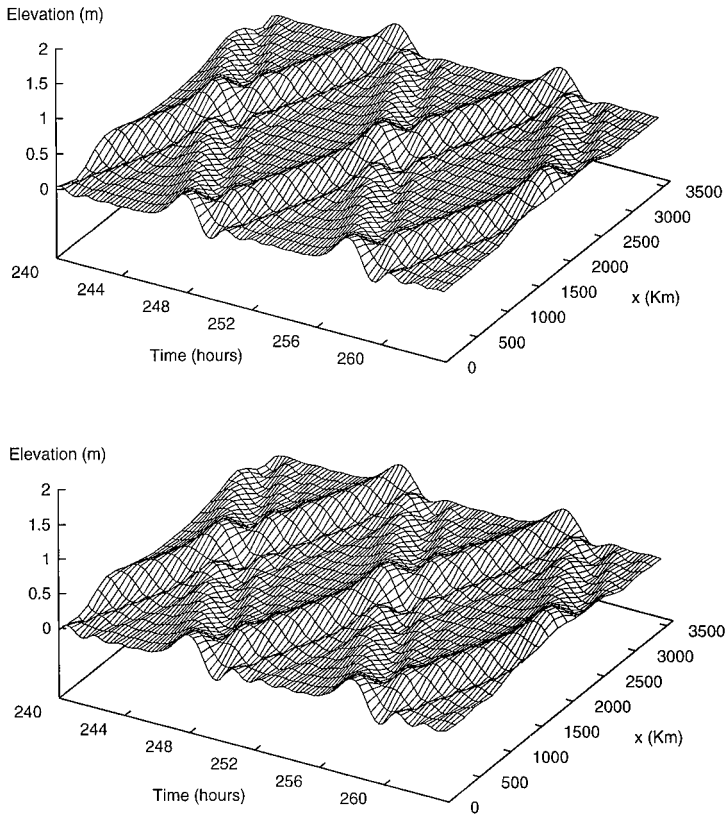
FIG. 7. Evolution of the free surface during day 10. Long waves are advanced using RK3 (top) and CN (bottom). In both cases, $\Delta t = 2$ min, $\Delta x = 10$ km, $\Delta X = 30$ km. The wave-CFL number on the coarse-grid $\text{CFL}_w = 0.396$.

step $\Delta t = 5$ min. The corresponding wave-CFL number on the coarse grid is $\text{CFL}_w = 0.996$. Figures 9 and 10 show that for $\Delta t = 5$ min, the CN and RK3 solutions exhibit noticeable differences. Compared with solutions obtained with $\Delta t = 2$ min, the RK3 solution shows that the shape of the waves is well preserved, with weak wave attenuation of the wave
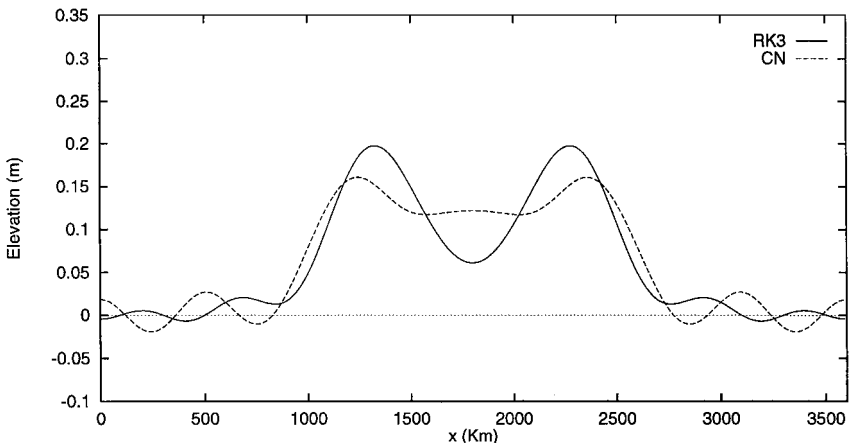

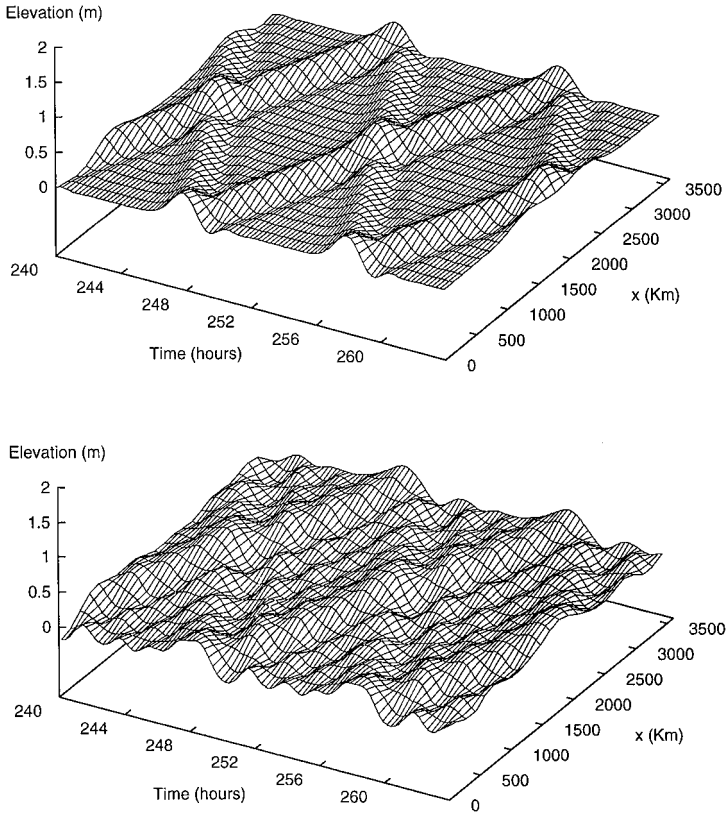**FIG. 8.** Comparison of RK3 and CN solutions at the end of day 10. Same parameters as in Fig. 7.

FIG. 9. Evolution of the free surface during day 10. Long waves are advanced using RK3 (top) and CN (bottom). In both cases, $\Delta t = 5$ min, $\Delta x = 10$ km, $\Delta X = 30$ km. The wave-CFL number on the coarse-grid $CFL_w = 0.996$.

amplitudes, which is particularly noticeable for the short-wavelength ripples. On the other hand, in the CN computation with $\Delta t = 5$ min phase errors build up substantially and the solution deteriorates rapidly. The present experiences indicate that, in the present fractional-step framework, the use of accurate explicit schemes to propagate long-wave data on coarse
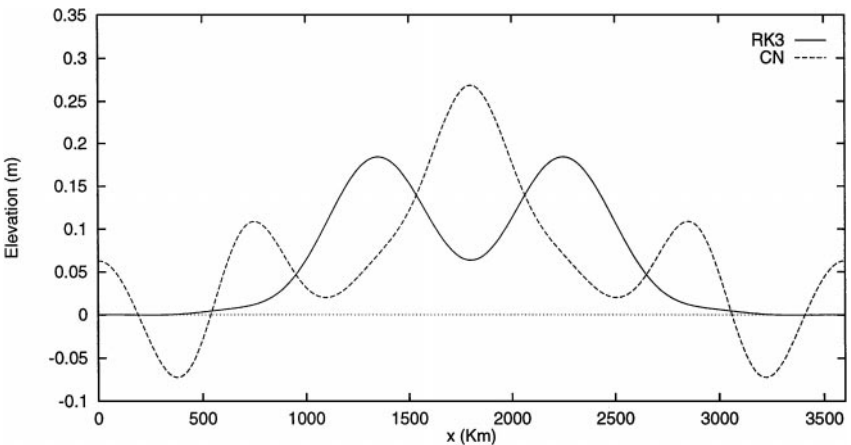

FIG. 10. Comparison of RK3 and CN solutions at the end of day 10. Same parameters as in Fig. 9.

grids is an attractive means to relax the integration time step while maintaining the quality of the solution.

4.3.4. *Effect of Grid Ratio*

The previous computations suggest that the coarse-grid resolution should be selected so that the corresponding wave-CFL number is not excessively large. This, in turn, suggests the use of a large grid ratio. However, as pointed out earlier, the grid ratio should be carefully selected, so that the filtered quantities are well represented. For the present centered-difference approximations, a reasonable estimate is to require roughly 10 points with the shortest cutoff wavelength, i.e., $10\Delta X_{max} \sim L_{ref}k_c$. For $k_c = 10$, $\Delta X_{max} \sim 36$ km.

To examine the effect of ΔX on the solution, computations are repeated using the RK3 scheme, $\Delta t = 2$ min, and $k_c = 10$. Three grid ratios are considered, $n_r = 3, 5$, and 9. The corresponding coarse-grid sizes are $\Delta X = 30, 50$, and 90 km, and the wave-CFL numbers are $CFL_w = 0.396, 0.237$, and 0.132. For $n_r = 3$, the solution is nearly identical to that obtained with $k_c = 15$, and shown in Figs. 7 and 8. For $n_r = 5$ and $n_r = 9$, the evolution of the free surface during day 10 is shown in Fig. 11; and the elevation at the end of day 10 is plotted in Fig. 12. The results indicate that as ΔX increases, the filtered fields may become poorly represented on the coarse grid, which results in severe deterioration in the accuracy of the solution.
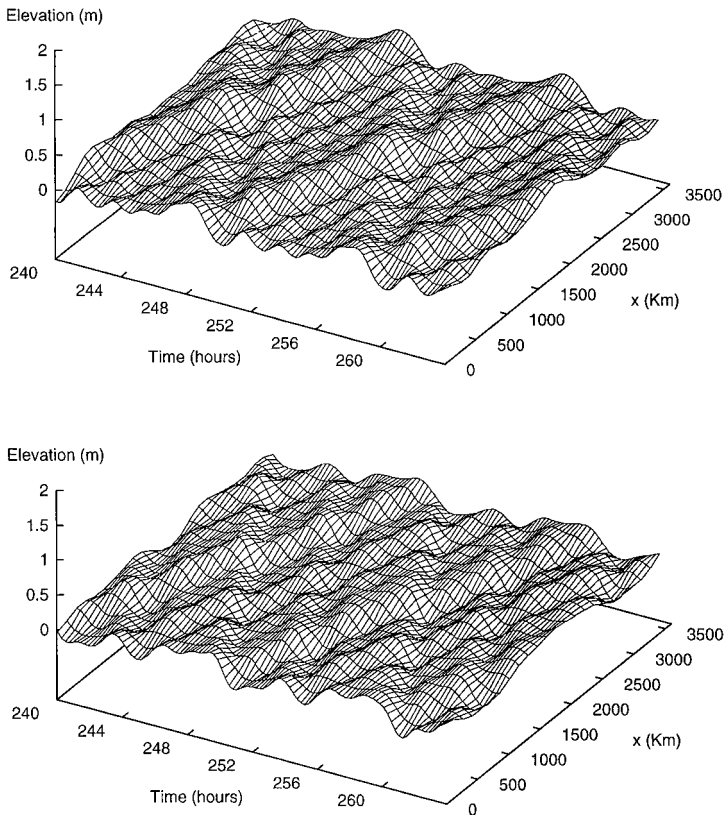

FIG. 11. Evolution of the free surface during day 10. Long waves are advanced using RK3 with $\Delta X = 50$ km (top) and $\Delta X = 90$ km (bottom). The corresponding grid ratios are $n_r = 5$ and $n_r = 9$, and the wave-CFL numbers $CFL_w = 0.237$ and 0.132, respectively. In both cases, $\Delta t = 2$ min, and $\Delta x = 10$ km.
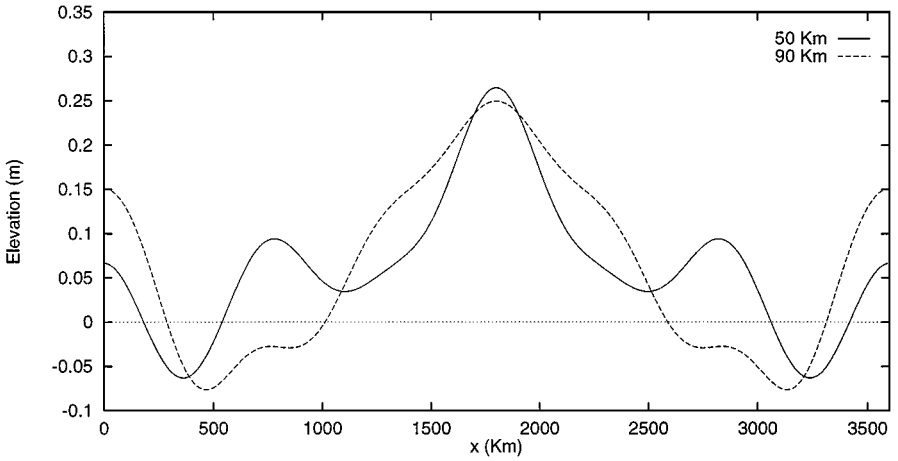
FIG. 12. Comparison of RK3 solutions after 10 days, using $\Delta X = 50$ km and $\Delta X = 90$ km. In both cases, $\Delta t = 2$ min, and $\Delta x = 10$ km.

The present computations indicate that the coarse-grid size should be selected to ensure adequate representation of filtered quantities. Generally, the coarse-grid size should be smaller than the filter size, and the required number of grid points for accurate discretization depends on the filter shape and on the type of spatial discretization. For the present centered-difference approximations and selected filter type, we find that about 8 grid points are sufficient to adequately capture all the dynamics up to the filter scale. This requirement may be relaxed if higher-order discretizations are used, and this provides additional motivation for the spectral-element discretization of the following section.

4.3.5. *Further Analysis of Behavior*

We conclude this section with a short remark on the behavior of the split scheme, particularly concerning the quality of the long-wave prediction. We briefly address this issue by comparing in Fig. 13 the free-surface elevation computed using the split scheme on a
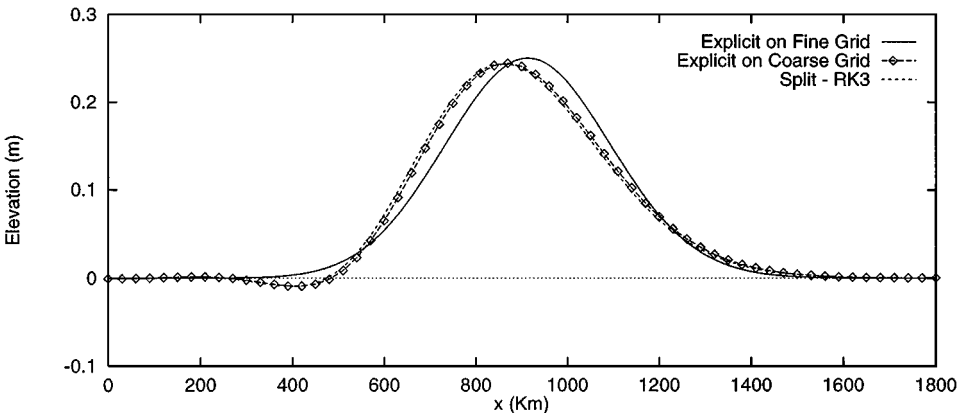

FIG. 13. Solutions at end of 2 days for the fully explicit schemes on coarse ($N = 120$) or fine ($N = 360$) grids and for the split scheme with the same coarse or fine grids. The explicit solutions are obtained with AB3 and $\Delta t = 10$ s. The split scheme uses RK3 for large-wave propagation and a design filter with $k_c = 15$. Only the left half of the domain is shown.

grid with $N_c = 120$ and $N_f = 360$ to predictions obtained using fully explicit schemes on grids with $N = 120$ and $N = 360$. The comparison shows that the prediction of the split scheme is very close to that obtained using the explicit scheme with $N = 120$. (Generally, we find a general agreement between the split and unsplit computations when the resolution of the coarse mesh in the split computations is the same as that of the unsplit scheme.) On the other hand, notable differences can be observed between the results of the split scheme at unsplit computations at finer resolution level, $N = 360$. These differences are due to the amplification of phase errors in the propagation of the surface gravity waves and not the result of splitting errors. To verify this claim, we first examine the effect of the time step by contrasting in Fig. 14 elevation profiles obtained with different values of Δt; the differences between the split and unsplit solutions are shown in Fig. 15. The results show that the predictions of both split and unsplit calculations are essentially independent of the value of the time step, indicating that differences observed in Fig. 13 are dominated by spatial (phase) errors. Combined with the above experiences, the present results indicate that the split scheme enables efficient prediction of long free-surface waves with an error level comparable to that of the unsplit computation at the coarse resolution level. Moreover, because of the implicit treatment at large CFL, the propagation of short waves on the fine grid may not be captured accurately. In practical situations, however, this does not lead to
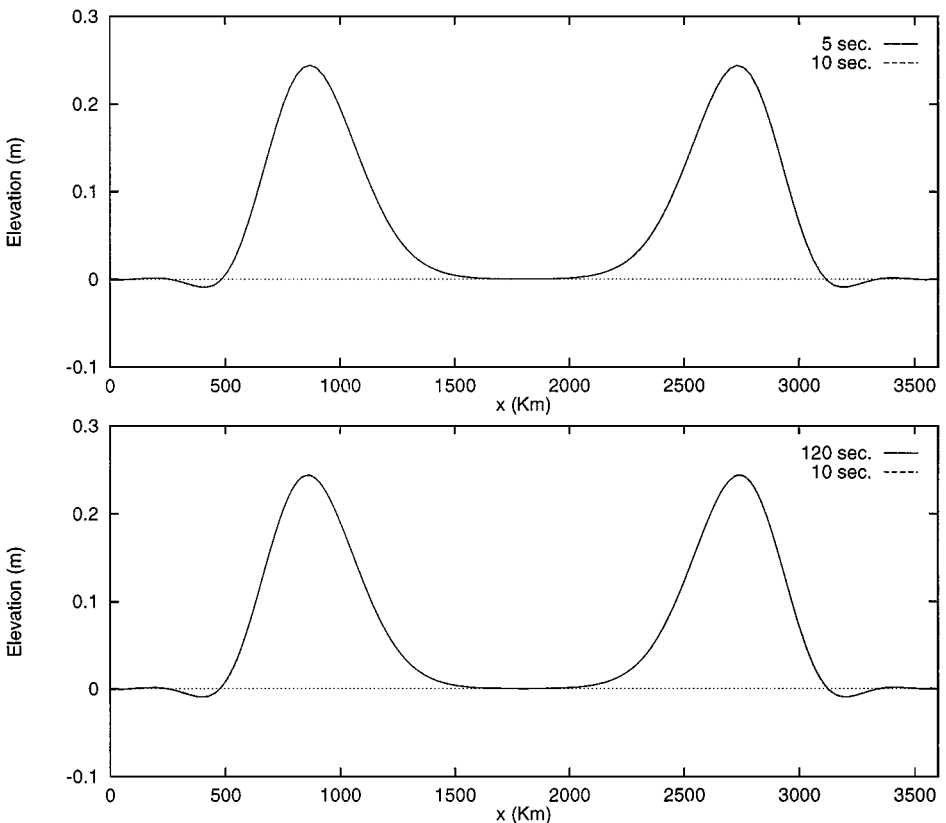

FIG. 14. Effect of the time step on the computed free-surface elevation for the fully explicit (top) and split (bottom) schemes. The explicit calculations are performed on a grid with $N = 120$, using AB3 integration with $\Delta t = 5$ and 10 s. The split scheme calculations are performed on a grid having $N_c = 120$ and $N_f = 360$, with time steps $\Delta t = 10$ and 120 s.
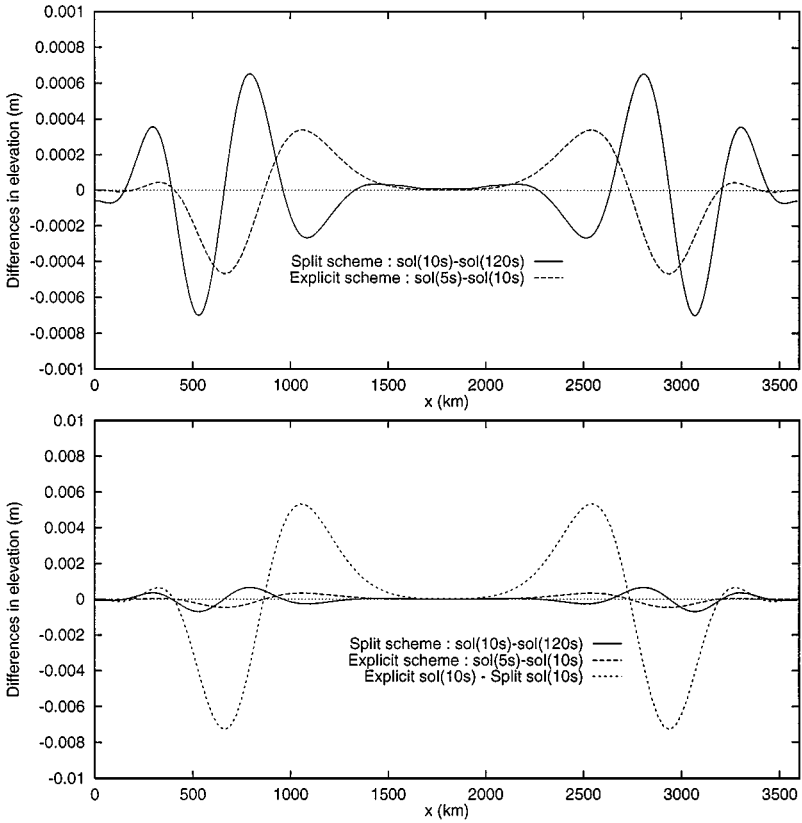
FIG. 15. Differences between the solutions given in Fig. 14.

major difficulty since short scales generally tend to be dominated by (nonlinear) advection phenomena.

Finally, we note that since the extraction of long waves is based on a convolution operation, the long-wave propagation may depend on the properties of the selected filter. We have performed a detailed study (not shown) to determine the effect of the filter on the predictions. We have found that the propagation of long waves and the corresponding phase errors depend only weakly on the choice of the filter when, first, the filter size is appropriately selected and, second, the large-scale component of the solution is well resolved on the coarse grid. In particular, the computations show that predictions obtained with the design filter are essentially identical to those obtained with a Fourier-spectral cutoff. By introducing noticeable damping at low wavenumbers, Gaussian-type filters do not fully capture the long-wave component of the solution and produce very small but noticeable differences from the spectral-cutoff and design filters. For these reasons, the design filter has been preferred.

5. SPECTRAL-ELEMENT COMPUTATIONS

Section 4 illustrated a finite-difference implementation of the splitting procedure proposed here. Its basic conclusions are (a) a double-grid method is necessary if an accurate representation of the large-scale wave is desired, (b) the errors in the split scheme are no

worse than those resulting from the unsplit integration of the equation on the same coarse grid, and (c) the filter must eliminate high-wavenumber features unresolvable on the coarse grid. With these lessons in mind, we proceed to investigate the implementation of the splitting scheme on a spectral-element discretization of the shallow-water equations.

The spectral-element method is an h-p type finite-element method that relies on high-order polynomials, usually of degree 4–11, to interpolate the solution within each element. It thus allows two paths to convergence: algebraic if the polynomial degree is held fixed while the number of elements is increased (h-refinement); and exponential if the elemental partition is held fixed and the degree of the interpolating polynomial is increased (p-refinement), and provided the solution is smooth. We present a very brief description of the spectral-element discretization in the following section, and we refer the reader to [19–24] for more details.

We focus below on the issues pertaining to the splitting procedure, namely the definitions of the fine and coarse grids, the transfer of information between the two grids, and the implementation of the averaging operator. We conclude this section with a series of numerical experiments to test the spectral-element version of the split scheme.

5.1. Spectral-Element Discretization

We present the spectral-element formulation for Eq. (2); the formulation for the individual split system can be derived similarly. The variational form of Eq. (2) is

$$\int_A \Phi u_t \, dA + \int_A \Phi \frac{1}{\epsilon^2} \nabla \zeta \, dA = \int_A (-u\nabla \cdot u + b)\Phi \, dA \tag{53}$$

$$\int_A \Psi \zeta_t \, dA - \int_A (h + \zeta)u \cdot \nabla \Psi \, dA = - \int_{\partial A} \Psi (h + \zeta)u \cdot n \, ds, \tag{54}$$

where Φ and Ψ are the test functions associated with the velocity and pressure, respectively. The divergence term in the continuity equation has been integrated by parts, and the boundary integral on the right-hand side of Eq. (54) represents the volume of fluid leaving the domain (n is the outward unit normal to the boundary); this integral is zero if the domain is closed.

The spectral-element discretization step relies on dividing the domain into elements in which the solution is interpolated. In 1D, the interpolation is expressed as

$$u(\xi) = \sum_{i=0}^{N} u_i h_i^v(\xi) \tag{55}$$

$$\zeta(\xi) = \sum_{i=0}^{N-2} \zeta_i h_i^p(\xi), \tag{56}$$

where h_i^v and h_i^p are the Legendre Cardinal functions [25] for the velocity and pressure grids, respectively. These are defined on the Gauss–Lobatto roots of the Legendre polynomials of degree N and $N - 2$. We have used a polynomial of lower order for the pressure in order to stagger the pressure and velocity collocation points, and thus suppress spurious pressure modes [12]. Setting $\Phi = h_i^v$ and $\Psi = h_i^p$, and substituting the interpolation formulas in the variational form, we obtain a system of ordinary differential equations in time which must be integrated according to the splitting procedure. We note that the integrals arising from

the variational form are evaluated with Gauss–Lobatto quadrature which leads to a diagonal mass matrix for the velocity and pressure. The time discretizations we have implemented are third-order Adams–Bashforth for System I, third-order Runge–Kutta for System II, and finally first-order Euler-Backward for System III.

5.2. Coarse Grids

The h-p character of the spectral element method offers severals approaches to coarsening the grid: p-coarsening, which consists of holding the elemental partition fixed while decreasing the degree of the polynomial, N; h-coarsening, where several elements are collapsed into one coarse element (element corners on the coarse grid are corners of elements on the fine grid); h-p coarsening, where the coarse elements are allowed to have a different spectral truncation than the fine grid; and, finally, a coarse grid where the elements' corners do not necessarily coincide with those of fine elements. (We do not pursue this last approach here as it does not extend easily to two dimensions.)

Experimentation has shown that p-coarsening alone is not flexible enough because of the (relatively) small number of spectral modes used in spectral-element methods and which, in practical circumstances, ranges from 4 to 11. In addition, the spectral truncation on the coarse elements cannot be made arbitrarily small without degrading the spectral properties of the numerical scheme.

We have studied two methods for the calculations of the coarse-grid fields. The first one is the convolution filter (26) and its associated transfer function defined in (52). The convolution integral is evaluated as a sum of elemental contributions which are calculated with Gauss–Lobatto quadrature; the procedure thus consists of elemental matrix–vector products. There are two drawbacks to the convolution approach that make it difficult to generalize to two dimensions. First, the weight function is only known in Fourier space through its transfer function H, which must be Fourier-transformed back to physical space. This inversion is in general difficult to calculate in two-dimensional domains with complicated geometries. In the present work, the weight function is evaluated on a dense equi-spaced grid via FFT before it is interpolated to the spectral-element collocation grid. Second, the storage of the convolution matrices increases as the square of the number of nodes in the grid, and becomes quickly impractical in two dimensions. Storage can be saved by taking advantage of the decaying character of the weight function and by discarding the contributions of nodes further away than a specified cutoff distance. This saving, however, is complicated to code, particularly in two-dimensional unstructured domains.

In order to circumvent the aforementioned difficulties, we have implemented a projection method to calculate the coarse-grid variables. This projection is essentially designed for the h-p coarsening where the corners of the coarse elements coincide with fine-element corners. The projection method is a modification of the mortar projection presented in Levin *et al.* [26]. Its highlights are that it operates at the coarse-element level, preserves the continuity of the function across coarse-element boundaries, and minimizes the difference between the coarse and fine representations. The following section describes the projection approach.

5.3. Projection Approach

Let $\bar{\Gamma}$ denote a coarse element comprising K fine elements Γ_k, $k = 1, \ldots, K$; see Fig. 16. Let $\bar{N}$ and N be the order of spectral interpolation on the coarse and fine grids, respectively.
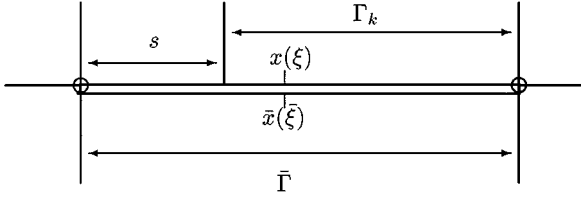
FIG. 16. Relative position of fine-element Γ_k within coarse-element $\bar{\Gamma}$; s is the offset between the corner of the coarse element and that of the fine elements. The fine and coarse elements have separate computational coordinates ξ and $\bar{\xi}$, respectively.

A function u on the fine grid admits a representation in terms of the N Legendre Cardinal functions:

$$u(x(\xi))|_{\Gamma_k} = \sum_{i=0}^{N} u_i^k h_i^N(\xi). \tag{57}$$

Its projection $\bar{u}$ onto the coarse element can be similarly written as a series of Legendre Cardinal functions of order $\bar{N}$:

$$\bar{u}(x(\bar{\xi})) = \sum_{m=0}^{\bar{N}} \bar{u}_m h_m^{\bar{N}}(\bar{\xi}). \tag{58}$$

Here, h_i^N and $h_m^{\bar{N}}$ denote the fine and coarse Legendre Cardinal functions defined on the Gauss–Lobatto roots of order N and $\bar{N}$, respectively. The projection is defined by the following:

$$\int_{\bar{\Gamma}} (\bar{u} - u)\psi \, dx = 0 \quad \forall \psi \in P(\bar{\Gamma})$$
$$\bar{u}(\bar{\xi} = -1) = u^1(\xi = -1) \tag{59}$$
$$\bar{u}(\bar{\xi} = 1) = u^K(\xi = 1).$$

Here, $P(\bar{\Gamma})$ denotes the space of polynomials defined on $\bar{\Gamma}$ of degree less than or equal to $\bar{N} - 2$. Relation (59) fixes the function values at the endpoints of the elements to those given on the fine grid and requires that $u - \bar{u}$ be orthogonal to the space $P(\bar{\Gamma})$; i.e., $\bar{u}$ and u have the same coefficients in the basis ψ_q. Note that because of the two constraints at the end points, only an additional $N - 2$ constraints can be imposed on $\bar{u}$.

The choice of basis for $P(\bar{\Gamma})$ is at our disposal, and, for convenience, we choose a set of modified Legendre Cardinal functions,

$$\psi_q(\xi) = \frac{-L'_{\bar{N}}(\xi)\left(1 - \xi_q^{\bar{N}}\right)\left(1 + \xi_q^{\bar{N}}\right)}{\bar{N}(\bar{N} + 1)L_{\bar{N}}\left(\xi_i^{\bar{N}}\right)\left(\xi - \xi_q^{\bar{N}}\right)}, \quad q = 1, \ldots, \bar{N} - 1, \tag{60}$$

where $L_{\bar{N}}$ is the Legendre polynomial of degree $\bar{N}$, and $\xi_q^{\bar{N}}, q = 1, \ldots, \bar{N} - 1$ are the roots of $L'_{\bar{N}}$. The ψ_q are polynomials of degree $\bar{N} - 2$, and also are the Lagrangian interpolants on the interior Gauss–Lobatto roots of $L_{\bar{N}}$, i.e., the coarse-grid collocation points minus the endpoints.

The discrete form of the projection operator is obtained by inserting (57) and (58) into (59):

$$\sum_{m=0}^{\bar{N}} \left(\int_{-1}^{1} h_m^{\bar{N}} \psi_q |x_{\bar{\xi}}| \, d\bar{\xi} \right) \bar{u}_m = \sum_{k=1}^{K} \sum_{i=0}^{N} \left(\int_{-1}^{1} h_i^{N} \psi_q |x_{\xi}^k| \, d\xi \right) u_i^k, \quad 1 \le q \le \bar{N} - 1$$

$$\bar{u}_0 = u_0^1, \tag{61}$$

$$\bar{u}_{\bar{N}} = u_N^K.$$

The $x_{\bar{\xi}}$ and x_{ξ}^k are the metric factors of the mapping between physical space and the computational spaces of the coarse and fine grids, respectively. The integrals on the left-hand side can be computed exactly with Gauss–Lobatto quadrature of order $\bar{N}$, provided x_{ξ} is (at most) a linear function. Similarly, the integrals on the right-hand side can be computed exactly with Gauss–Lobatto quadrature of order N in each element of the fine grid provided that $N \ge \bar{N}$. Equations (61) are $\bar{N} + 1$ equations in the $\bar{N} + 1$ unknowns $\bar{u}_m$. Note that the choice of quadrature and weight functions produces a diagonal matrix on the right-hand side, thus reducing the operation count needed for the projection. The latter can thus be written compactly as a matrix vector product of the form

$$\bar{u}_q = \sum_{k=1}^{K} \sum_{i=0}^{N} Q_{qi}^k u_i^k, \quad 0 \le q \le N. \tag{62}$$

The formulas for the Q_{qi}^K are listed in the Appendix.

5.4. Numerical Experiments

5.4.1. *Periodic Channel*

Here, we reconsider the periodic channel problem of Section 4.1, but with a modified initial condition of the form

$$u(x, t = 0) = 0, \quad \zeta(x, t = 0) = 0.5 \exp\left[\frac{-1}{0.005} \left(\frac{x}{L} - \frac{1}{2}\right)^2\right] + 0.05 \sin\left(\frac{2\pi x}{\lambda}\right). \tag{63}$$

The initial wave form is made up of two distinct waves, a large-scale Gaussian hump with a decay length scale of $\sqrt{0.005}L = 255$ km and amplitude of 0.5 m, and a small-scale sine wave with one-tenth the amplitude with wavelength $\lambda = 120$ km. The Fourier spectrum of the surface displacement has very small Fourier coeffcients ($< 1.10^{10}$) for all Fourier modes $n > 21$, except $n = 31$, where there is a single spike. This separation in spectral space allows us to call the first part the large wave, and the other part the small wave. The remaining physical parameters of the problem are set to $L = 3600$ km, $D = 1000$ m, and $g = 10$ m/s². The wave speed is $\sqrt{gh} = 100$ m/s; hence the wave needs 10 h to return to its initial position.

The aim of the numerical simulations reported here is to assess the ability of the split scheme to propagate the large-scale wave properly, to investigate the sensitivity of the solution to the method used to transfer information between the coarse and fine grids (filter versus projection method), and finally to experiment with the different coarsening strategies. To compare quantitatively the different numerical experiments, we define an error measure that focuses primarily on the large-scale component of the wave. This large-scale component is extracted by padding the spectrum of the solution with zero for all modes higher than 21.

TABLE I

			Unsplit		Split filter		Split projection	
$\bar{K}$	$\bar{N}$	Δt	ϵ_∞	ϵ_2	ϵ_∞	ϵ_2	ϵ_∞	ϵ_2
24	15	10	1.60e-3	1.21e-5				
24	11	20	1.50e-3	1.16e-5	1.40e-3	1.50e-5	1.60e-3	1.22e-5
24	9	40	1.90e-3	1.36e-5	1.59e-3	1.51e-5	1.70e-3	1.19e-5
24	7	60	4.80e-3	2.86e-5	2.64e-3	2.36e-5	2.40e-3	1.68e-5
24	5	150	4.70e-2	2.88e-4	2.19e-3	1.40e-4	1.57e-2	8.54e-5
24	3	400	4.09e-1	3.30e-3	4.37e-1	2.98e-3	4.47e-1	3.90e-3

Note. p-coarsening, fine grid has $K = 24$ and $N = 15$; the coarse grid has $\bar{K} = 24$. ϵ_2 refers to the rms error in the surface elevation, and ϵ_∞ to the maximum error.

Tables I, II, and III summarize the results of our numerical experiments for the p, h, and mixed h-p coarsening, respectively. Three solutions are computed for each set of coarsening experiment: a reference solution using the original unsplit scheme computed on the coarse grid of the split scheme, and two split scheme solutions using either the design filter or the projection method to transfer information between the fine and coarse grids. (The filter parameters were held fixed at $k_c = 10$ and $n_c = 1$.) In addition, we have dropped the nonlinear terms from the shallow-water equations for this particular set of experiments, and all errors reported herein used the analytical solution to the linearized equations as a reference.

We note that the elemental partition of the fine grid consists of 24 150-km elements, with each element holding 1.25 small waves. Using Boyd's rule of thumb [25], $N = 5 + 4(M − 1)$, where M is the number of waves within an element, the small waves are resolved to better than 1% accuracy on the fine grid for $N \geq 7$. None of the coarse grids listed in the tables can resolve the small-scale wave, except for the p-coarsening case with $\bar{N} \geq 7$. We also note that as N increases, the spectral-element model becomes more spectral in character, and the minimum grid spacing decreases as $1/N^2$; thus the most stringent CFL restriction is encountered for $K = 24$ and $N = 15$.

Examination of maximum and rms errors in Tables I–III reveals that the numerical errors of the split scheme are similar to those of the coarse-grid unsplit scheme; thus the errors introduced by the splitting are small. The tables also reveal that the split scheme allows a substantially larger time step without incurring an undue penalty in the accuracy of the

TABLE II

			Unsplit		Split filter		Split projection	
$\bar{K}$	$\bar{N}$	Δt	ϵ_∞	ϵ_2	ϵ_∞	ϵ_2	ϵ_∞	ϵ_2
24	9	40	1.90e-3	1.36e-5				
12	9	80	1.06e-2	6.20e-5	3.10e-3	2.00e-5	6.40e-3	4.72e-5
8	9	120	2.91e-2	2.26e-4	5.32e-3	3.20e-5	2.78e-2	3.95e-4
6	9	160	5.37e-2	3.36e-4	1.10e-1	1.65e-3	2.19e-2	1.55e-4
4	9	240	1.07e-1	7.18e-4	9.08e-1†	8.72e-2†	7.34e-2	5.80e-4

Note. h-coarsening, fine grid has $K = 24$ and $N = 9$; the coarse grid has $\bar{N} = 9$. Simulations marked with a † were unstable due to a leakage of small-scale wave onto the coarse-grid solution.

TABLE III

			Unsplit		Split filter		Split projection	
$\bar{K}$	$\bar{N}$	Δt	ϵ_∞	ϵ_2	ϵ_∞	ϵ_2	ϵ_∞	ϵ_2
12	7	120	3.20e-2	2.64e-4	5.36e-3	3.78e-5	1.94e-2	2.59e-4
12	5	300	1.40e-1	9.35e-4	4.76e-1	6.98e-3	8.29e-2	6.65e-4
8	7	200	8.17e-2	7.92e-4	3.25e-2	2.16e-4	3.87e-2	6.65e-4
8	5	450	2.10e-1	1.50e-3	†	†	2.10e-1	1.80e-3
6	7	250	1.13e-1	7.42e-4	†	†	5.00e-1	4.00e-3
6	5	600	2.59e-1	1.80e-3	†	†	3.10e-1	2.60e-3

Note. h-p coarsening, fine grid has $K = 24$ and $N = 9$. Simulations marked with a † were unstable due to a leakage of small-scale wave onto the coarse-grid solution.

large-scale wave. This is particularly true when there is a large difference in spectral truncation between the coarse and fine grids (Table I); however, we note that the errors deteriorates rapidly for $\bar{N} < 7$ becase of increased numerical dispersion errors, and become unacceptable for $\bar{N} = 3$. The increase in allowable time step is smaller for the h-coarsening case (Table II) and grows in proportion to $\bar{K}^{-1}$.

The filter and projection split schemes behave similarly for the p-coarsening case, with both schemes producing an accurate estimate of the large-scale component of the wave. The filter's performance in the h-coarsening experiment is mixed: it produces smaller errors than the projection for $\bar{K}$ equal to 24 and 12, and worse errors for $\bar{K} < 8$. The explanation of this behavior resides in the choice of filter parameters in (52) which were held fixed at $k_c = 10$ and $n_c = 1$. The filter scheme yields accurate results as long the coarse grid can resolve a Fourier mode of wavenumber less than or equal to k_c. Using Boyd's rule of thumb, this translates into a requirement on $\bar{N}$ of the form $\bar{N} \geq 5 + 4(k_c/\bar{K} - 1)$. Alternatively, one can choose $k_c = (\bar{N} + 1)\bar{K}/4$ to guarantee a well-resolved wave on the coarse grid, an issue that we do not pursue here. The projection method displays a more robust behavior because it adapts automatically to the coarse-grid resolution.

The present numerical experiments demonstrate that the split scheme improves the stability limit imposed by the wave speed, particularly when there is a large difference between the spectral truncations of the fine and the coarse grid. They also demonstrate that the coarse-grid spectral truncation must be greater than 4 in order to produce an accurate estimate of the large-scale waves. The optimum coarse grid for the present problem is the h-p coarsened grid with $\bar{K} = 8$ and $\bar{N} = 7$. It provides for an acceptable error level and a fivefold increase in the time step.

5.4.2. *Long-Time Integration*

The ability of the split scheme to propagate the large-scale waves for long time is illustrated by integrating the previous example for 30 days. The fine grid in this example consists of 24 elements of order 9, and the coarse grid of 8 elements of order 7. The initial condition is as before but without the small-scale perturbations. We compare the results of the split scheme with those obtained from an unsplit explicit integration whose time step respects the wave-CFL condition on the fine grid. Figure 17 show the results of the split integration with $\Delta t = 240$ s and $\Delta t = 120$ s, together with the results of the explicit integration with $\Delta t = 40$ s. The splitting scheme shows good agreement with the fully explicit scheme with
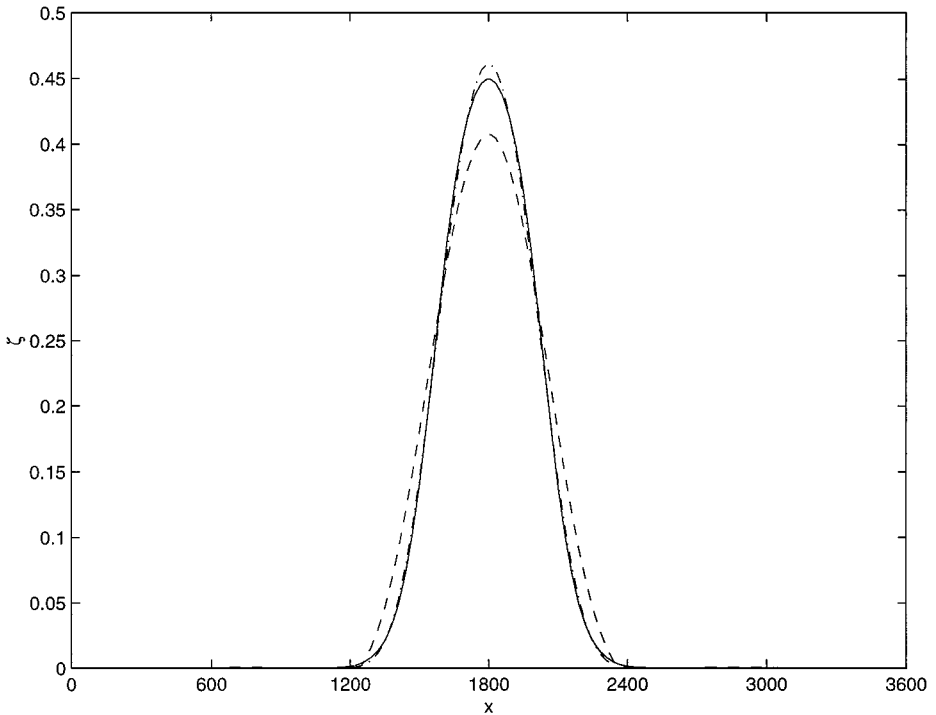
FIG. 17. Surface elevation after 30 days of integration with the split scheme with two different time steps: (−−) $\Delta t = 240$ s, and (−·−) $\Delta t = 120$ s, and with explicit scheme using (—) $\Delta t = 40$ s.

regard to the phase speed of the wave. However, the wave amplitude in the split scheme displays a slight decay, which decreases with the time step. This decay is mainly due to the integration of the short waves by the dissipative backward Euler scheme. To verify this, we perform the standard semi-implicit integration of the unsplit wave system using a backward Euler for the gravity terms. As shown in Fig. 18, the semi-implicit scheme has effectively dissipated the solution after just 1 day, while both explicit and split schemes preserve much of the amplitude of the solution.

5.4.3. *Variable Bathymetry*

The presence of topography can lead to wave generation, and it is therefore important to test the split scheme in the presence of topography. Consistent with the assumptions in the asymptotic analysis, we consider only large-scale topographic variations. Figure 19 shows the topography chosen for the present experiment. The depth consists of the superposition of an exponential "hill" with a sine wave of mode 4. Note that the sine wave leads to a nonsymmetric profile and that the depth variations exceed 50% of the mean depth.

The initial perturbation of the free surface is the large-scale wave of the previous test problem, but centered on the first third of the computational domain. A 2-min time step is chosen; the remainder of the numerical parameters are as follows: the coarse grid has 24 elements with $N = 14$, the coarse grid has 10 elements with $\bar{N} = 9$, and the cutoff wavenumber has been set to 12 and n_c to 1. These values lead to a $\mathrm{CFL_w}$ equal to 0.82 based on a reference depth of 1000 m.
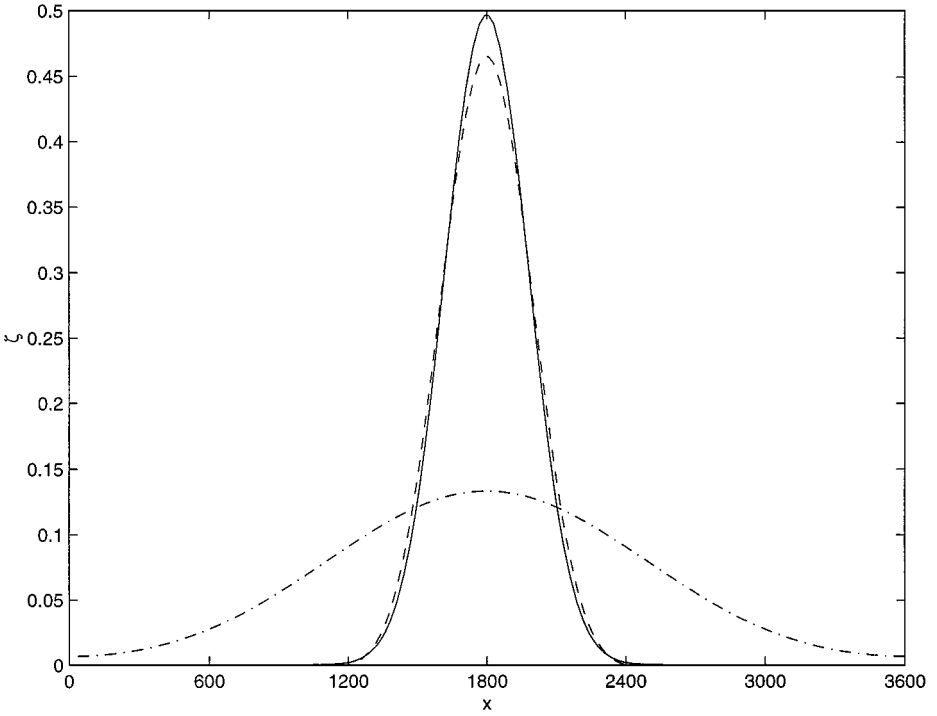
FIG. 18. Surface elevation after 5 days of integration with the split scheme using $\Delta t = 240$ s (– –), the unsplit semi-implicit scheme using $\Delta t = 240$ s (–·–), and the unsplit explicit scheme using $\Delta t = 40$ s (—).

The time evolution of the free surface is plotted in Fig. 20. The results show that wave propagation is substantially affected by depth variation. As in the previous cases, left- and right-propagating components of the initial perturbation are still clearly tractable, but in the present case the generation of new modes can be observed. Note also that for the time scale considered (1 day), the evolution seems to be roughly periodic with characteristic period close to $L_{\text{ref}}/\sqrt{gH_{\text{ref}}} \approx 10$ h.

5.4.4. *Wall Boundary Conditions*

The implementation of the averaging and filtering operators in the examples above depended implicitly on the periodicity conditions. These operators must be modified for nonperiodic boundary conditions in order to prevent the support of the weight function from extending outside the computational domain. The modified averaging and filtering
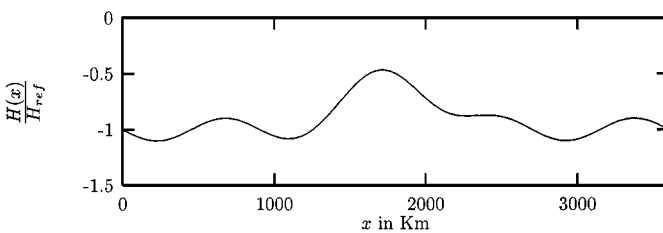

FIG. 19. Normalized depth for computational case of Section 5.4.4.
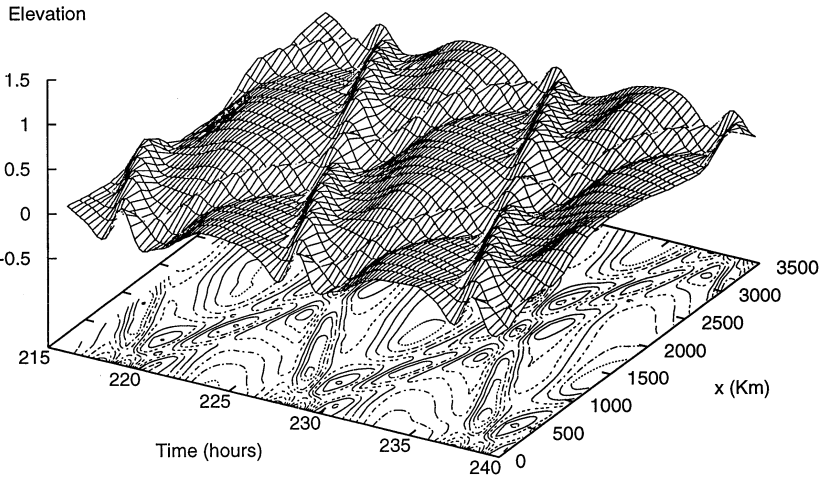
FIG. 20. Evolution of the free-surface perturbation during day 9 for periodic and variable test case. Depth profile is given in Fig. 19. $\Delta t = 2$ min, and $k_c = 12$.

operators must also be able to handle one-sided averaging footprints near the boundary. This is easily implemented in one-dimensional problems by truncating the convolution of the fields with W and renormalizing the truncated weight function. The performance of the truncated averaging operator is briefly illustrated by considering the same domain and initial conditions as in the previous example, but with the perdiocity velocity conditions replaced with homogeneous Dirichlet boundary conditions. The evolution of the free-surface perturbation is plotted in Fig. 21. It shows that the truncated averaging operator in the closed domain does not introduce spurious oscillations. The loss of spatial periodicity is clearly visible, as neither the initial conditions nor the depth profile is symmetric.
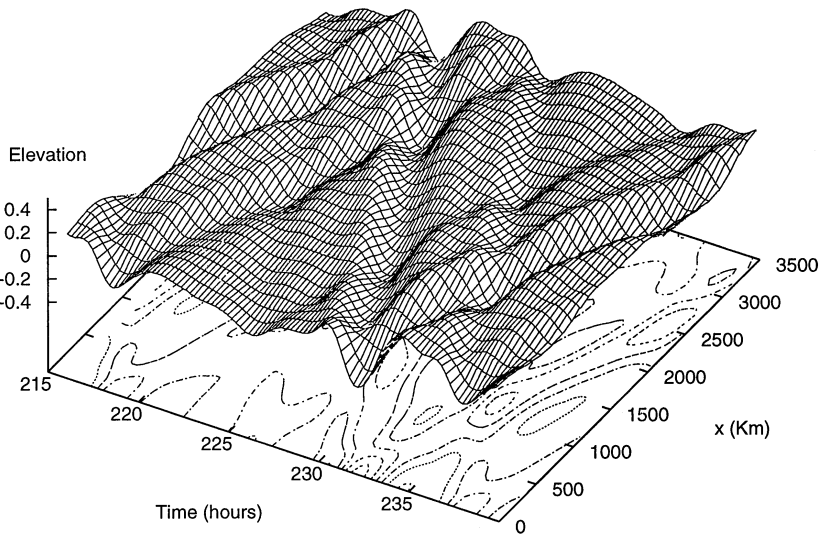

FIG. 21. Evolution of the free-surface perturbation during day 9 for the wall boundary conditions and variable depth. The depth profile is given in Fig. 19. $\Delta t = 2$min, and $k_c = 12$.

The truncation of the weight function and renormalization are much harder to implement for two-dimensional problems, particularly if the basin geometry is complicated and if the grid is unstructured. The difficulties stem from the facts that, first, the transfer function H in Eq. (52) cannot be inverted easily to obtain W_d, and, second, the storage requirement would increase subtantially. We note, finally, that the projection operator does not depend on periodicity because it operates locally at the (coarse) element level, and because it does not modify the boundary values.

6. CONCLUSION

We have exploited our multiple-scale analysis of the shallow-water equations to design a new multiple-pressure-variable (MPV) solver that is effective in defeating the stifiness from the high speed of surface gravity waves. Our MPV approach splits the barotropic pressure, i.e., the surface elevation, into three components that are integrated separately. The first component, dubbed the slow mode, responds to slow dynamics such as internal wave motion and advection. The second component is the large-scale pressure responding to the fast dynamics of the surface gravity wave. The third component is the small-scale pressure that also corresponds to the fast, "near-equilibrium" dynamics of the surface wave.

We have constructed finite-difference and spectral-element versions of our MPV shallow-water solver. The two versions yield similar results and confirm that the splitting of the pressure succeeds in defeating the stability limit imposed by the surface gravity waves regardless of the underlying spatial discretization.

The integration of the large-scale pressure requires the formation of a coarse mesh where the CFL limit on the fast gravity waves would be comparable to the convective CFL limit on the original grid. This coarsening can be achieved in one of three ways in SEOM: p-coarsening, where the elemental partition would be kept the same and the order of the interpolation polynomial would be reduced to linear; h-coarsening, where the interpolation order would be kept constant but a coarse element would be formed from the union of several fine elements; and finally a combination of h-p coarsening. Our experiments revealed that pure p-coarsening is not a viable choice because the accuracy of the scheme deteriorated and became unacceptable when linear or quadratic interpolation was used. These low-order interpolations introduced a large dispersive numerical error that distorted the propagation of the large-scale pressure wave. This error became insignificant as soon as the degree of the interpolation polynomial exceeded 5. We have thus adopted an h-p coarsening strategy that bunches fine elements together to form the coarse element and that keeps the interpolation order comparable to the one in the original fine grid.

The calculation of the large-scale pressure requires the application of a suitable averaging and filtering operator with good spectral properties on the coarse grid, i.e., one that eliminates all small-scale structures since these adversely affect the integration step. While Gaussian-type averaging operators proved to be adequate, computed results showed that the spectral-like design filter is superior, particularly for the finite-difference version. For spectral elements, the spectral averaging is limited since "global spectra" on complex domains with unstructured grids are difficult to form. We have thus relied on the local spectrum at the coarse element level in order to segregate the large-scale signal from the small-scale component. We have devised a projection-type method, borrowed from the mortar-element method, to transfer information between the coarse and fine grids. This projection has good interpolation and stability property and has been retained in our code.

We have adopted the following integration schemes for each component in the solution: (a) an explicit third-order Adams–Bashforth scheme (AB3) for advection terms, (b) a third-order Runge–Kutta scheme (RK3) for the large-scale pressure mode, and (c) an implicit Crank–Nicholson scheme (CN2) or a first-order Euler-Backward scheme (EB) for the small-scale pressure mode. The RK3 proved to be superior to CN2 for the large-scale pressure mode because it has substantially less dispersive errors and has acceptable stability properties. For the small-scale pressure mode, the CN2 proved to be adequate for the finite-difference version but unstable for the spectral-element version. This was traced back to the dissipation properties of the CN2 scheme when the time step exceeded the explicit stability limit by a large factor. In this regime, small-scale waves are underdamped by CN2 and can lead to a buildup of energy at the tail-end of the spectrum and thus to unstable behavior. The spectral-element version turned out to be more sensitive to such aliasing than the finite-difference version, and thus required the adoption of a more stable integration scheme such as EB.

In summary, our numerical experiments with the one-dimensional version have allowed us to finalize our choices for the coarsening strategy, averaging and filtering operators to compute the large-scale signals, and the integration schemes for each pressure mode. The splitting algorithm has been extended to two dimensions and is currently being tested.

APPENDIX

The evaluation of the integrals involves the mappings between the computational spaces of the fine and coarse elements and physical space. The two mappings are linked by $x(\bar{\xi}) = x(\xi)$ for $x \in \Gamma_k$, where $\bar{\xi}$ is the computational coordinate in the coarse element, and ξ is the computational coordinate in the fine element. In one-dimensional problems where the elements are stretched linearly only, we have the relation

$$\bar{\xi}(\xi) = \frac{2}{|\bar{\Gamma}|}s - 1 + \frac{|\Gamma_k|}{|\bar{\Gamma}|}(\xi + 1), \tag{64}$$

where $|\bar{\Gamma}|$ is the length of the coarse element, $|\bar{\Gamma}_k|$ is the length of the fine element, and s is an offset between the two (see Fig. 16).

The entries of the projection matrix are given by

$$Q_{0i}^k = \delta_{i0}\delta_{k1} \tag{65}$$

$$Q_{qi}^k = \frac{\psi_q(\bar{\xi}(\xi_i))\omega_i^N|x_\xi^k|_i - \delta_{i0}\delta_{k1}u_0^1 B_0 \psi_q(-1) - \delta_{iN}\delta_{kK}u_N^K B_{\bar{N}}\psi_q(1)}{B_q}, \quad 1 < q < \bar{N} \tag{66}$$

$$Q_{\bar{N}i}^k = \delta_{i0}\delta_{k1} \tag{67}$$

$$B_q = \omega_q^{\bar{N}}|x_{\bar{\xi}}|_q, \tag{68}$$

where $\omega_i^{\bar{N}}$ and ω_i^N are, respectively, the $\bar{N}$th and Nth order Gauss-Lobatto quadrature weights, $|x_{\bar{\xi}}|_q$ is the metric of the transformation between physical space and the coarse-element computational space evaluated at $\bar{\xi}_q$, $|x_\xi^k|_i$ is the corresponding fine-element metrics evaluated at ξ_i^k, and δ_{mn} is the Kronecker delta.

ACKNOWLEDGMENTS

REFERENCES

1. K. Bryan, A numerical method for the study of the circulation of the world ocean, *J. Comput. Phys.* **4**, 347–376 (1969).

2. D. B. Haidvogel, J. L. Wilken, and R. Young, A semi-spectral primitive equation ocean circulation model using vertical sigma and orthogonal curvilinear horizontal coordinates, *J. Comput. Phys.* **94**, 151–185 (1991).

3. J. K. Dukowicz, R. D. Smith, and R. C. Malone, A reformulation and implementation of the Bryan–Cox–Semtner ocean model on the connection machine, *J. Atmospheric Oceanic Technol.* **10**, 195 (1993).

4. N. Pinardi, A. Rosati, and R. C. Pacanowski, The sea-surface pressure formulation of rigid lid models. Implications for altimetric data assimilation studies, *J. Mar. Syst.* **6**, 110–119 (1995).

5. R. L. Higdon, and R. A. de Szoeke, Barotropic-baroclinic time splitting for ocean circulation modeling, *J. Comput. Phys.* **135**, 30–53 (1997).

6. R. L. Higdon, Implementation of a Barotropic-baroclinic time splitting for isopycnic coordinate ocean modeling, *J. Comput. Phys.* **148**, 579–604 (1999).

7. R. Hallberg, Stable split time stepping schemes for large-scale ocean modeling, *J. Comput. Phys.* **135**, 54–65 (1997).

8. R. L. Higdon and A. F. Bennett, Stability analysis of operator splitting for large-scale ocean modelling, *J. Comput. Phys.* **123**, 311–329 (1996).

9. J. K. Dukowicz and R. D. Smith, Implicit free-surface method for the Bryan–Cox–Semtner ocean model, *J. Geophys. Res. C* **99**, 7991 (1994).

10. Y. Wang and K. Hutter, A semi-implicit semispectral primitive equation model for lake circulation dynamics and its stability performance, *J. Comput. Phys.* **139**, 209–241 (1998).

11. R. Klein, Semi-implicit extension of a Godunov-type scheme based on low-Mach-number asymptotics. I. One-dimensional flow, *J. Comput. Phys.* **121**, 213–237 (1995).

12. M. Iskandarani, D. B. Haidvogel, and J. P. Boyd, A staggered spectral element model with application to the oceanic shallow water equations, *Int. J. Numer. Meth. Fluids* **20**, 393–414 (1995).

13. O. Le Maître, M. Iskandarani, J. Levin, and O. M. Knio, A multiple scales pressure splitting of the shallow-water equations II. Two-dimensional tests, in preparation (2001).

14. A. S. Worlikar, O. M. Knio, and R. Klein, Numerical simulation of a thermoacoustic refrigerator, *ESAIM Proc.* **1**, 363–375 (1996).

15. O. M. Knio, A. S. Worlikar, and H. N. Najm, Mixing and chemical reacting in an idealized swirl chamber, in Twenty-Sixth Symposium (International) on Combustion (The Combustion Institute, 1996), pp. 203–209.

16. A. Majda and J. Sethian, The derivation and numerical solution of equations for zero Mach number combustion, *Comb. Sci. Tech.* **42**, 185–205 (1985).

17. T. S. Schneider, N. Botta, K.-J. Geratz, and R. Klein, Extension of finite volume compressible solvers to multi-dimensional, variable-density zero Mach number flows, *J. Comput. Phys.,* in press.

18. C.-D. Munz, S. Roller, R. Klein, and K.-J. Geratz, The extension of incompressible flow solvers to the weakly compressible regime, *Theoret. Comput. Fluid Modeling,* submitted for publication.

19. A. T. Patera, A spectral element method for fluid dynamics: Laminar flow in a channel expansion, *J. Comput. Phys.* **54**, 468–488 (1984).

20. E. M. Ronquist, Ph.D. thesis. (Massachusetts Institute of Technology, Cambridge, 1988).

21. G. E. Karniadakis, Spectral element simulation of turbulent flows in complex geometries, *Appl. Numer. Math.* **6**, 85–105 (1989).

22. H. Ma, A spectral element basin model for the shallow water equations, *J. Comput. Phys.* **109**, 133–149 (1993).

23. M. Taylor, J. Tribbia, and M. Iskandarani, The spectral element method for the shallow water equations on the sphere, *J. Comput. Phys.* **130**, 92–108 (1997).

24. J. Levin, M. Iskandarani, and D. B. Haidvogel, A spectral filtering procedure for eddy-resolving simulations with a spectral element ocean model, *J. Comput. Phys.* **137**, 130–154 (1997).

25. J. P. Boyd, *Chebyshev and Fourier Spectral Methods, Lecture Notes in Engineering* (Springer-Verlag, New York, 1989).

26. J. Levin, M. Iskandarani, and D. B. Haidvogel, A nonconforming spectral element ocean model, *Int. J. Numer. Meth. Fluids* **34**, 495–525 (2000).